MIMS Technical Report No.00047 (201504061)

Homogenization and fingering instability of a microgravity smoldering combustion problem with radiative heat transfer

Ekeoma Rowland Ijioma[a,c,*], Hirofumi Izuhara[d], Masayasu Mimura[a,b,c], Toshiyuki Ogawa[a,b,c],

[a] *Meiji Institute for Advanced Study of Mathematical Sciences (MIMS), Meiji University, 4-21-1 Nakano, Nakano-ku, Tokyo, 164-8525, Japan*
[b] *Graduate School of Advanced Mathematical Sciences, Meiji University, 4-21-1 Nakano, Nakano-ku, Tokyo, 164-8525, Japan*
[c] *Center for Mathematical Modeling and Applications (CMMA), Meiji University, 4-21-1 Nakano, Nakano-ku, Tokyo, 164-8525, Japan*
[d] *Faculty of Engineering, University of Miyazaki, 1-1 Gakuen Kibanadai-nishi, Miyazaki 889-2192, Japan*

Abstract

The present study concerns the homogenization and fingering instability of a microgravity smoldering combustion problem with radiative heat transfer. The major premise of the homogenization procedure is the slow exothermic fuel oxidation of a reactive porous medium at the pore level. The porous medium consists of ϵ-periodically distributed cells, with ϵ a suitable scale parameter. A nonlinear reaction rate of Arrhenius type accounts for the relationship between the reactants and the heat that sustains the smoldering process. At the gas-solid interface, the balance of thermal fluxes is given by the heat production rate due to the reaction and the radiative heat losses at the interface. Since the size of the inclusions is small with respect to ϵ, we derive a kinetic model for fuel conversion in the region occupied by the solid inclusions and hence complete the description of a single-step chemical kinetics. The derived macroscopic model shows a close correspondence to a previous phenomenological reaction-diffusion model, within a suitable choice of parameters. We perform numerical simulations on the microscopic and

*Corresponding author
Email addresses: e.r.ijioma@gmail.com (Ekeoma Rowland Ijioma), hiro.izuhara@gmail.com (Hirofumi Izuhara), mimura.masayasu@gmail.com (Masayasu Mimura), tshogw@gmail.com (Toshiyuki Ogawa)

homogenized models in order to verify the efficiency of the homogenization process in the slow smoldering regime. We also show that the results of the macroscopic model capture the distinct fingering states reminiscent of microgravity smoldering combustion.

Keywords: multiscale modelling, homogenization, smoldering combustion, radiative heat transfer, fingering instability

---

1. Introduction

The mathematical modeling of reactive processes in porous media has been a subject of enormous interest, specifically, due to the nature of the chemical processes involved. In addition, there is an inherent difficulty usually encountered when attempting to resolve the details of the pertinent porous medium of interest. A typical example of such a problem concerns the slow exothermic chemical reaction taking place on the surface of reactive porous materials, in the presence of a gaseous mixture containing an oxidizer. When the chemical process proceeds in a non flaming mode, it is referred to as smoldering. Distinct configurations of smoldering are possible depending on the direction of flow of the gaseous oxidizer relative to the direction of propagation of the reaction front. These configurations have been a subject of practical interest since they exhibit some important characteristic features. If the gaseous oxidizer flows in a direction opposite to the direction of the reaction front, we refer to the configuration as reverse (upstream) smoldering, whereas if the oxidizer flows in the same direction as the direction of propagation, the configuration is known as forward (downstream) smoldering. For a detailed discussion on the distinct smoldering configurations, we refer to Ohlemiller and Lucca (1983); Ohlemiller (1985); Wahle et al. (2003); Schult et al. (1995).

Furthermore, it has been reported in several experimental papers (Zik et al., 1998; Zik and Moses, 1999, 1998; Olson et al., 1998, 2006; Kuwana et al., 2014), that the smoldering process occurring under microgravity results in the self-fragmentation of the smolder front. The phenomenon was believed to arise from a destabilizing effect of oxygen transport in the absence of natural convection, which characterizes a microgravity environment. The smolder front has the form of finger-like patterns, which are distinct depending on the oxygen velocity (or its concentration). The experimental results were further validated mathematically in different contexts (Lu and Yortsos, 2005; Kagan and Sivashinsky, 2008; Ikeda and Mimura, 2008; Fasano et al., 2009; Ijioma et al., 2013; Yuan and Lu, 2013; Hu et al., 2015; Kuwana

et al., 2014; Ijioma et al., 2015; Uchida et al., 2015). For a mathematical aided understanding of the smoldering combustion problem, a traveling wave analysis of the pertinent mathematical model is usually adopted (see Kagan and Sivashinsky, 2008; Fasano et al., 2009, e.g.). The interest is to determine the range of the experimental observation through the analysis of the spread rate of the smoldering front.

The derivation of macroscopic behavior of porous media combustion from pore level has been achieved over the past years using either of two approaches. The first approach involves a volume averaging method (Whitaker, 1998), which has been applied in the derivation of filtration combustion models (see Oliveira and Kaviany, 2001, for instance). However, until now, there has been no mathematical justification of the validity of the volume averaging approach from the pore level. The second approach uses the homogenization theory (Bakhvalov and Panasenko, 1989; Bensoussan et al., 1978; Sanchez-Palencia and Zaoui, 1985; Hornung, 1997), which has the advantage of making the model derivation mathematically rigorous. In Ijioma et al. (2013, 2015), a macroscopic model of the smoldering combustion problem was derived using the method of periodic homogenization and its rigorous justification via the two-scale convergence method (Allaire, 1992; Allaire et al., 1995) was discussed in Fatima et al. (2014). The model emphasizes the role of conductive heat transfer in the system without heat losses to the surroundings, and hence cannot be used for answering questions concerning the influence of heat losses. The homogenization of heat transfer processes has attracted the attention of researchers over the years; see for instance Auriault (1997); Monsurro (2003) for a treatment of conductive heat transfer scenarios. In Allaire and El Ganaoui (2009); Allaire and Habibi (2013), processes involving conductive and radiative heat transfers in porous media with cavities were studied. We also point out some of the studies on radiative heat transfer in the literature (Kagan and Sivashinsky, 1996, 1997, for instance).

The physical (or rather experimental) setup of the problem is as shown in Figure 2 (cf. Zik and Moses, 1999; Kuwana et al., 2014). It consists of an upper gas layer and a lower solid layer in which the porous sample is placed. A gaseous mixture is supplied from one end of the setup and ignition is initiated at the other end, thus allowing a reverse smoldering combustion to proceed. The region of interest may be simply taken to be two-dimensional along the direction of flow of the gaseous mixture, which occupies a homogeneous gas layer since the thickness of the sample is negligibly small. An alternative point of view for a two-dimensional approximation is the fact that the smoldering combustion process we have in mind takes place in a

narrow gap (Zik et al., 1998; Zik and Moses, 1999; Kuwana et al., 2014). The size of the gap ensures the absence of natural convection and hence draws the problem much closer to a variant of the phenomenon observed under microgravity (Olson et al., 1998). In the latter report, it is shown that, within a suitable range of oxidizer velocity, it is possible for the smoldering propagation to proceed downstream after the smolder front reaches the upstream end of the sample. The result is the subsequent smoldering of parts of the unburned fuel left behind by the upstream smolder wave.

Regarding the description of the microstructure of the porous medium, we consider a situation in which the gaseous oxidizer is free to infiltrate the porous medium through diffusion and convective transport. That is, instead of a perforated domain consisting of a solid matrix (see Figure 1a), we take the solid fibers to be distributed in a gas matrix (see Figure 1b). An advantage of this microstructure is that it allows simultaneous treatment of coupled heat and mass transfer problem in the heterogeneous porous medium consisting of seemingly distinct reference microstructures for the two transport processes. The next challenge concerns the description of the microstructure for the purpose of homogenization. We assume that the region for homogenization, depicted in Figure 3, consists of a uniformly periodic distribution of ϵ-sized cells, with ϵ being the size of the period. The sizes of the ϵ-periodically distributed cells are assumed to be increasingly small. In view of the complexity of the chemical reactions taking place on the distributed ϵ-scaled surfaces, a direct numerical simulation of the problem at this level becomes almost unattainable and far too costly in terms of computer resources. Also, it is impossible to capture the qualitative behavior of the phenomena experimentally observed at the macroscopic level while attempting to resolve all the details of the processes occurring at the microstructure level. Thus, the present goal of homogenization in this pa-

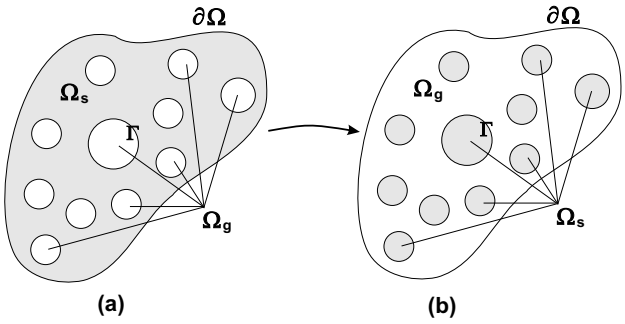

Figure 1: Schematic of the physical porous medium (a) perforated domain with solid matrix, Ω_s and holes Ω_g with boundary Γ; (b) gas-solid domain with gas matrix Ω_g and solid inclusions Ω_s with boundary Γ.

per is to derive a functional form of the limit homogenized problem in order

to overcome the difficulty of dealing with the intricate structure and chemical processes of the heterogeneous porous medium. Additionally, explicit formulas for calculating the effective transport parameters have to be derived as well. The effective parameters allow us to show the efficiency of the homogenization process (cf. Ijioma, 2014). Contrary to the models derived earlier (Ijioma et al., 2013; Fatima et al., 2014; Ijioma et al., 2015), the novelty of the present study is the introduction of heat transfer by radiation and a kinetic model for solid fuel mass concentration. The kinetic model involves a second order Arrhenius type nonlinearity in the problem. Based on these improvements, we show that the results of the proposed model are within a suitable range for describing the experimentally observed fingering behavior of smoldering combustion under microgravity. The organization of this paper is as follows:

Contents

2. Pore scale description of the problem

In this section, we discuss the derivation of the microscopic model for a smoldering combustion problem with a one-step kinetic scheme.

2.1. Geometry of the porous medium

Let $\Omega := \prod_{j=1}^{2}(0, L_j)$ be a smooth bounded open set in $\mathbb{R}^2$, which is subdivided into $N(\epsilon)$ periodicity cells $Y_i^\epsilon, i = 1, \cdots, N(\epsilon)$, with each cell being equal and defined up to a translation of a reference cell $Y := \prod_{i=1}^{2}(0, l_j)$. The number of cells with respect to ϵ, in each coordinate direction j, is defined by $N_j(\epsilon) := |L_j|\,\epsilon^{-1}, j = 1, 2$, where L_j define the lengths of the sides of the domain Ω. Then, the total number of cells in the domain Ω is $N(\epsilon) := N_1(\epsilon) \times N_2(\epsilon)$. Here, $\epsilon := l/L$ is the size of a single period cell defined as the ratio of the characteristic length of Y to the characteristic length of the domain Ω. The reference cell consists of two distinct parts- a gas filled part and a solid part. We denote by Y_s, the solid part of Y having a smooth boundary denoted by Γ. The gas filled part is denoted by $Y_g := Y \setminus \overline{Y_s}$. The collection of the periodically distributed solid parts is given by $Y_{s,i}^\epsilon, i = 1, \cdots, N(\epsilon)$. Similarly, the collection of the periodically distributed boundaries of $Y_{s,i}^\epsilon$ is denoted by $\Gamma_i^\epsilon, i = 1, \cdots, N(\epsilon)$. Thus, the ensemble of the periodically translated solid parts, the matrix of gas parts and the ensemble of the solid boundaries can be written as

$$\Omega_s^\epsilon := \bigcup_{i=1}^{N(\epsilon)} Y_{s,i}^\epsilon, \quad \Omega_g^\epsilon := \Omega \setminus \overline{\Omega_s^\epsilon}, \quad \Gamma^\epsilon := \bigcup_{i=1}^{N(\epsilon)} \Gamma_i^\epsilon. \tag{1}$$

Let us now denote by $|\cdot|$, the measure of any of the sets introduced above. Specifically, $|Y|$ is the volume measure of the reference cell Y, with $|\Gamma|$ the surface measure of Γ. We also note that the measures on the periodic cells can be represented in terms of the measures on the reference cells through the following relation:

$$|Y_i^\epsilon| = \epsilon^2 |Y|, \quad |\Gamma_i^\epsilon| = \epsilon |\Gamma|, \text{ for } i = 1, \cdots, N(\epsilon).$$

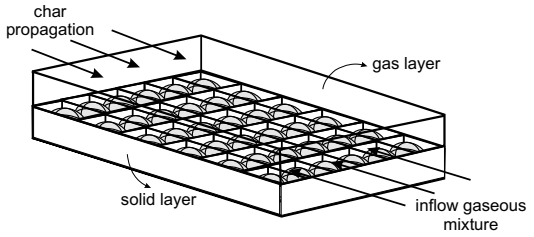

Figure 2: Schematic diagram of the three dimensional gas-solid geometry.

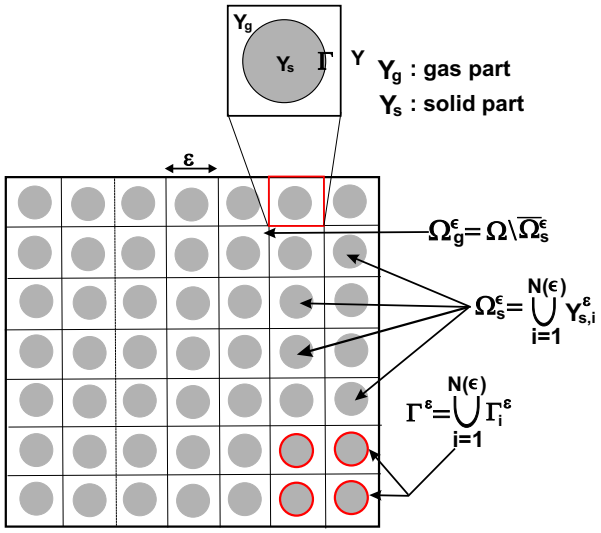

Figure 3: Two dimensional periodic domain for homogenization and the reference cell.

2.2. Chemistry of the problem

The model of heterogeneous chemical reactions for smoldering combustion can be described by using the kinetic schemes given by Rogers and Ohlemiller (1980), which has been widely employed in numerical simulations of smolder processes (Leach et al., 2000; Aldushin et al., 2006, 2009). Here, the chemical kinetics is governed by a single step kinetic scheme for fuel oxidation, i.e.

$$\text{Solid fuel} + \mu_{1o} O_2 \xrightarrow[Q_1]{W_1} \mu_{1c}\text{Char} + \mu_{1gp}\ \text{Gaseous products}, \tag{2}$$

where W_1 is the reaction rate and Q_1, the heat release. The stoichiometric coefficients are denoted by μ_{1i}. The oxidation reaction (2) is exothermic (i.e. $Q_1 > 0$). The rate law governing (2) is given by

$$W_1 = P^\epsilon C^\epsilon A_1 \exp(-E_1/RT_s^\epsilon), \tag{3}$$

where P^ϵ is the mass concentration of the solid fuel, C^ϵ is the concentration of gaseous oxidizer, which is usually Oxygen, T_s^ϵ is the temperature of the solid, E_1 is the activation energy, R is the universal gas constant and A_1, the pre-exponential factor in the Arrhenius law. The rate law given by (3) is second order with respect to the reactants species. This is one of main extensions to the models of first order rate law studied (see Ijioma et al., 2013, 2015; Kuwana et al., 2014; Kagan and Sivashinsky, 2008, e.g) for a similar smoldering combustion scenario.

2.3. Balance equations for heat and mass transport

We consider a diffusion-convection problem describing the transport of mass of a gaseous mixture, which is coupled to a heat transport problem. One of the properties of the medium is that the diffusion coefficients are varying in space, i.e. the coefficients take only two different values of the same order of magnitude. The gaseous oxidizer occupies the subdomain, $\Omega_{\mathrm{g}}^{\epsilon}$, and reacts with the solid inclusions (i.e. solid fuel) at the surface Γ^{ϵ}. Let the thermal conductivity of the constituent parts be defined by the constants λ_{g} and λ_{s}. Hence, we denote the conductivity coefficient λ^{ϵ} of the medium Ω by

$$\lambda^{\epsilon}(x) = \lambda_{\mathrm{g}}\chi_{\mathrm{g}}\left(\frac{x}{\epsilon}\right) + \lambda_{\mathrm{s}}\chi_{\mathrm{s}}\left(\frac{x}{\epsilon}\right),\ x \in \Omega, \tag{4}$$

where $\chi_{\mathrm{i}}, i = g, s$, are characteristic functions. Similarly, the volumetric heat capacity, $\mathcal{C}^{\epsilon}$, is defined by

$$\mathcal{C}^{\epsilon}(x) = \mathcal{C}_{\mathrm{g}}\chi_{\mathrm{g}}\left(\frac{x}{\epsilon}\right) + \mathcal{C}_{\mathrm{s}}\chi_{\mathrm{s}}\left(\frac{x}{\epsilon}\right),\ x \in \Omega. \tag{5}$$

Convection of the gaseous oxidizer only takes place in the gaseous subdomain $\Omega_{\mathrm{g}}^{\epsilon}$. Thus, we define it as follows

$$\mathbf{u}^{\epsilon}(x) = \begin{cases} 0, & x \in \Omega_{\mathrm{s}}^{\epsilon}, \\ \mathbf{V}^{\epsilon}(x), & x \in \Omega_{\mathrm{g}}^{\epsilon}, \end{cases} \tag{6}$$

where (6) implies the restriction of convection to the gaseous subdomain Ω_{g}^{ϵ}. We assume a spatially periodic flow, i.e. $\mathbf{u}^{\epsilon}(x) = \mathbf{u}(x, \frac{x}{\epsilon})$ in $\Omega_{g}^{\epsilon}, y = x/\epsilon$. The molecular diffusion of the gaseous mixture is restricted to $\Omega_{\mathrm{g}}^{\epsilon}$. Let the temperature in the periodic domain Ω be denoted by T^{ϵ}, which can be decomposed as

$$T^{\epsilon}(t,x) = \begin{cases} T_{\mathrm{s}}^{\epsilon}(t,x), & x \in \Omega_{\mathrm{s}}^{\epsilon}, \\ T_{\mathrm{g}}^{\epsilon}(t,x), & x \in \Omega_{\mathrm{g}}^{\epsilon}, \end{cases}$$

where T^{ϵ} is continuous on the interface Γ^{ϵ}. Besides the continuity of temperature across the interface, we also have the balance of heat fluxes given by the heat produced due to reaction at the interface and radiative heat losses to the surroundings, i.e. the following conditions, for the balance of heat, are satisfied across the interface

$$\begin{aligned} -\lambda_{\mathrm{g}}\nabla T_{\mathrm{g}}^{\epsilon}\cdot n &= -\lambda_{\mathrm{s}}\nabla T_{\mathrm{s}}^{\epsilon}\cdot n \\ &\quad +\epsilon Q_1 W_1 - \epsilon\sigma(T_{\mathrm{s}}^{\epsilon,4} - T_{\infty}^{4}),\ x \in \Gamma^{\epsilon}, t > 0, \\ T_{g}^{\epsilon} &= T_{s}^{\epsilon}, \end{aligned} \tag{7}$$

where $\sigma, Q_1 > 0$ are given constants denoting the radiative heat transfer and the heat release coefficients. The linear form of (7) with respect to the radiative transfer term is given by

$$-\lambda_{\mathrm{g}} \nabla T_{\mathrm{g}}^{\epsilon} = -\lambda_{\mathrm{s}} \nabla T_{\mathrm{s}}^{\epsilon} \cdot n + \epsilon Q_1 W_1 - \epsilon\sigma(T_{\mathrm{s}}^{\epsilon} - T_{\infty}),\ x \in \Gamma^{\epsilon}, t > 0. \tag{8}$$

The ϵ scaling of the terms on the right hand side of (8) is chosen as described in Ijioma et al. (2013, 2015). It ensures that the desired homogenized model with radiative heat transfer is obtained when passing to the limit $\epsilon \to 0$. We also assume that the following equations hold respectively for the consumption of the gaseous oxidizer and the solid fuel across the interface:

$$D\nabla C^{\epsilon} \cdot n = -\epsilon W_1 = \epsilon \frac{\partial P^{\epsilon}}{\partial t}, \quad x \in \Gamma^{\epsilon}, t > 0. \tag{9}$$

The initial and external boundary conditions are given by

$$\begin{cases} T^{\epsilon}(0,x) = T_0(x), C^{\epsilon}(0,x) = C_0, & x \in \Omega, \\ P^{\epsilon}(0,x) = P_0(x), & x \in \Gamma^{\epsilon}, \\ \partial_{x_1} T^{\epsilon}(t,x) = 0, C^{\epsilon}(t,x) = C_0, & x_1 = L_1, t > 0, \\ \partial_{x_1} T^{\epsilon}(t,x) = 0, \partial_{x_1} C^{\epsilon}(t,x) = 0, & x_1 = 0, t > 0, \\ \partial_{x_2} T^{\epsilon}(t,x) = 0, \partial_{x_{x2}} C^{\epsilon}(t,x) = 0, & x_2 = 0, x_2 = L_2, t > 0. \end{cases} \tag{10}$$

Remark 2.1. *So far, the description of the microscopic problem involves only fuel oxidation at the surface, Γ^{ϵ}. However, fuel conversion within the region, Ω_s^{ϵ}, is yet to be accounted for. In the sequel, we describe, under a set of assumptions, the complete kinetic model for a single step reaction mechanism.*

2.4. Complete kinetic model for the solid fuel mass balance

According to (2), a single step kinetic scheme is considered for the fuel consumption, i.e. fuel oxidation, on the surface Γ^{ϵ}. However, for a complete description of mass balance of P^{ϵ}, the fuel conversion within the inclusions is described by using the information provided by its consumption rate on the surface. The basic assumption for the chemical conversion in the inclusions invokes the notion of fuel pyrolysis within the inclusions. To model this effect, the following assumptions denoted by $\mathcal{A}$ are necessary:

Assumptions

($\mathcal{A}_1$) P^{ϵ} is consumed due to fuel oxidation on the surface, Γ^{ϵ}.

($\mathcal{A}_2$) At the level of the inclusions (assumed relatively small), the rate of fuel conversion in each $Y^\epsilon_{s,i}$ is given by the average rate of fuel oxidation on $\Gamma^\epsilon_i, i = 1, \cdots, N(\epsilon)$.

($\mathcal{A}_3$) The overall rate of fuel conversion in Ω^ϵ_s is balanced by the first order average rate of consumption on Γ^ϵ.

We proceed as follows: the rate of change of fuel in Ω^ϵ_s is given by

$$\frac{\partial P^\epsilon}{\partial t} = -k^\epsilon_{1_i} \tilde{P}^\epsilon_i, \quad x \in \Omega^\epsilon_s, i = 1, \cdots, N(\epsilon), \tag{11}$$

where we define the fuel content in each $Y^\epsilon_{s,i}$ according to

$$\tilde{P}^\epsilon_i := \begin{cases} \dfrac{1}{|\Gamma^\epsilon_i|} \displaystyle\int_{\Gamma^\epsilon_i} P^\epsilon dS, & \text{in } Y^\epsilon_{s,i}, \text{ for each } i, \\ 0, & \text{in } \Omega^\epsilon_g \end{cases} \tag{12}$$

and

$$k^\epsilon_{1_i} := \frac{A_1}{|\Gamma^\epsilon_i|} \int_{\Gamma^\epsilon_i} C^\epsilon \exp(-E_1/RT^\epsilon_s) dS, \text{ in } Y^\epsilon_{s,i}, i = 1, \cdots, N(\epsilon) \tag{13}$$

by assumption ($\mathcal{A}_2$). The rate of fuel oxidation is given by

$$\frac{\partial P^\epsilon}{\partial t} = -k^\epsilon_2 P^\epsilon, \qquad x \in \Gamma^\epsilon, \tag{14}$$

where $k^\epsilon_2 = C^\epsilon A_1 \exp(-E_1/RT^\epsilon_s)$, with the additional condition that $k^\epsilon_{1_i} = k^\epsilon_2, i = 1, \cdots, N(\epsilon)$, on Γ^ϵ, according to ($\mathcal{A}_3$), i.e.

By defining a first order rate law as:

$$k^\epsilon_2 := A_1 C^\epsilon \exp(-E_1/RT^\epsilon_s), \qquad x \in \Gamma^\epsilon, \tag{15}$$

we average (15) over Γ^ϵ and thus obtain the following

$$\frac{1}{|\Gamma^\epsilon|} \int_{\Gamma^\epsilon} k^\epsilon_2 dS = \frac{1}{|\Gamma^\epsilon|} \int_{\Gamma^\epsilon} A_1 C^\epsilon \exp(-E_1/RT^\epsilon_s) dS \tag{16}$$

$$= \sum_{i=1}^{N(\epsilon)} \frac{A_1}{|\Gamma^\epsilon_i|} \int_{\Gamma^\epsilon_i} C^\epsilon \exp(-E_1/RT^\epsilon_s) dS \tag{17}$$

$$= \sum_{i=1}^{N(\epsilon)} k^\epsilon_{1_i}, \tag{18}$$

where $k^\epsilon_{1_i} \in Y^\epsilon_{s,i}, i = 1, \cdots, N(\epsilon)$ due to ($\mathcal{A}_2$).

Remark 2.2. *Alternatively, one can simply take the rate of change of fuel in Ω_s^ϵ to be given by*

$$\frac{\partial P^\epsilon}{\partial t} = -k_{1_i}^\epsilon P^\epsilon, i = 1, \cdots, N(\epsilon), \tag{19}$$

where the rate coefficient, $k_{1_i}^\epsilon$, is given by (13).

Collectively, in terms of the scale parameter, ϵ, the microscopic system of equations has the following form:

$$\begin{cases} \mathcal{C}_{\rm g}\dfrac{\partial T_{\rm g}^\epsilon}{\partial t} = \mathcal{C}_{\rm g}\mathbf{u}^\epsilon\cdot\nabla T_{\rm g}^\epsilon + \nabla\cdot(\lambda_{\rm g}\nabla T_{\rm g}^\epsilon), & x\in\Omega_{\rm g}^\epsilon, t>0,\\ \mathcal{C}_{\rm s}\dfrac{\partial T_{\rm s}^\epsilon}{\partial t} = \nabla\cdot(\lambda_{\rm s}\nabla T_{\rm s}^\epsilon), & x\in\Omega_{\rm s}^\epsilon, t>0,\\ \dfrac{\partial C^\epsilon}{\partial t} = \mathbf{u}^\epsilon\cdot\nabla C^\epsilon + \nabla\cdot(D\nabla C^\epsilon), & x\in\Omega_{\rm g}^\epsilon, t>0,\\ \dfrac{\partial P^\epsilon}{\partial t} = -\displaystyle\sum_{i=1}^{N(\epsilon)} k_{1_i}^\epsilon \tilde{P}_i^\epsilon, & x\in\Omega_s^\epsilon, t>0,\\ -\lambda_{\rm g}\nabla T_{\rm g}^\epsilon\cdot n = -\lambda_{\rm s}\nabla T_{\rm s}^\epsilon\cdot n \ + & \\ \epsilon Q_1 W_1^\epsilon + \epsilon\sigma(T_\infty - T_{\rm s}^\epsilon), & x\in\Gamma^\epsilon, t>0,\\ T_g^\epsilon = T_s^\epsilon, & x\in\Gamma^\epsilon, t>0,\\ -D\nabla C^\epsilon\cdot{\rm n} = -\epsilon W_1^\epsilon = \epsilon\dfrac{\partial P^\epsilon}{\partial t}, & x\in\Gamma^\epsilon, t>0. \end{cases} \tag{20}$$

2.5. Numerical study of the microscopic model

In this section, our objective is to show that the essential physics of the phenomenon of interest is well-captured at the pore level. Specifically, we show that the radiative heat transfer at the pore surfaces and the effect of a second order reaction rate, which gives rise to upstream and downstream waves, are captured by the pore scale description.

To fix ideas, we assume that the lengths of the porous medium in each coordinate direction are $L_1 = 5$ cm and $L_2 = 1$ cm. We choose the characteristic length of the domain to be $L = 5$ cm. Then, by using the scaling argument, $\epsilon = l/L = 0.2$, with $l = 1$ cm, the number of cells in each coordinate direction can be calculated as:

$$N_1(\epsilon) = \epsilon^{-1}\left|L_1\right| = 25, N_2(\epsilon) = \epsilon^{-1}\left|L_2\right| = 5, \tag{21}$$

so that the total number of cells in the medium is given by $N(\epsilon) = N_1(\epsilon)\times N_2(\epsilon) = 125$. Here, we have assumed that the $\mathbb{R}^2$ space is partitioned with

ϵ-multiples of the standard periodicity cell. We also assume that the domain size is sufficiently large to suffice our model of radiative heat transfer. However, we have chosen the length, L_2, of the domain in the transversal direction to be relatively small in order to minimize the total number of cells in the system. Thus, periodic boundary conditions are imposed on the lateral boundaries.

The numerical method for the discretization of the problem uses the standard Galerkin method with Lagrange $P2$ finite elements. The time integration of the resulting discrete system of equations was performed with a Backward Differentiation Formula (BDF) as implemented in COMSOL Multiphysics package. The typical scaled parameter values used in the numerical simulations include: $\lambda_g = 2.38 \times 10^{-4}, \lambda_s = 7 \times 10^{-4}, D = 0.25, \mathcal{C}_g = 1.57 \times 10^{-3}, \mathcal{C}_s = 0.69, T_a = E_1/R = 1.0, Q_1 = 2.5, A_1 = 0.5, \sigma = 8.5 \times 10^{-3}, V = 1 \times 10^{-2}$.

We choose the following initial condition for T^ϵ:

$$T^\epsilon(0,x) = T_0 \exp\left(-x^2/\mu\right), \text{ with } T_0, \mu > 0 \text{ in } \Omega, \tag{22}$$

and for C^ϵ and P^ϵ, we choose

$$C^\epsilon(0,x) = 0.23, \quad \text{in } \Omega_g^\epsilon, \quad P^\epsilon(0,x) = 1.0, \quad \text{in } \overline{\Omega_s^\epsilon}. \tag{23}$$

In order to prevent negative values in the variable P^ϵ, we use the following definition in the numerical implementation:

$$\widetilde{P^\epsilon} := \begin{cases} \delta, & P^\epsilon < 1, \\ P^\epsilon, & 0 \le P^\epsilon \le 1, \\ 1, & P^\epsilon > 1. \end{cases} \tag{24}$$

where $\delta > 0$ is a very small number.

First, let us consider the microscopic model (20) with no radiative heat transfer, i.e. $\sigma = 0$. Figure 4 depicts the solid fuel conversion in this case. The structure of the combustion waves is given in Figures 4b, 4d, 4f and 4h. The values of C^ϵ and T^ϵ have been scaled with their maximum values to aid visibility of the waves. Figure 4 delineates the coexistence of upstream and downstream smolder waves, as expected from the use of the second order reaction rate. Figures 4a-4d show upstream smolder waves whereas Figures 4e-4h illustrate the downstream waves. Ignition is initiated from the left and the oxidizer gas is supplied from the upstream boundary (the right end), and hence allowing reverse (counterflow) smoldering combustion waves to emanate. The waves propagate initially upstream. On reaching the right

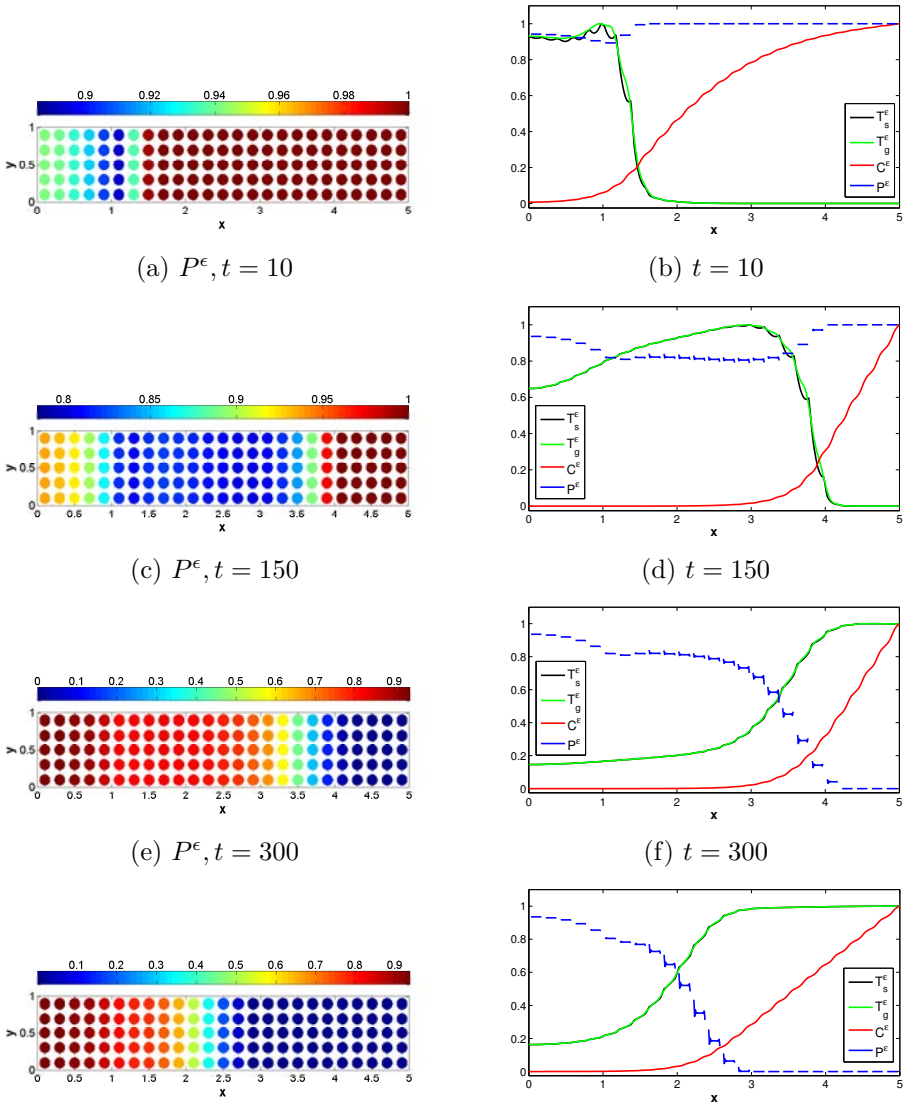

(a) $P^\epsilon, t = 10$ (b) $t = 10$

(c) $P^\epsilon, t = 150$ (d) $t = 150$

(e) $P^\epsilon, t = 300$ (f) $t = 300$

(g) $P^\epsilon, t = 600$ (h) $t = 600$

Figure 4: Evolution of the spatial profiles of solid fuel concentration P^ϵ (a), (c) (respectively (e), (g)) with their corresponding wave structures; (b), (d) upstream smolder waves (respectively (f), (h) downstream smolder waves). Ignition is initiated from the left and inlet oxidizer gas flows from the right. The circular color pattern indicates regions of unburned fuel (dark red) and regions of burned fuel (remaining colors with blue indicating higher conversion of the fuel).

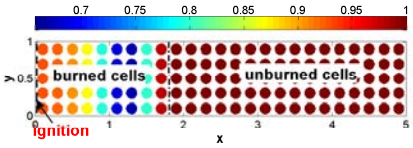

(a) $P^\epsilon, t = 10$

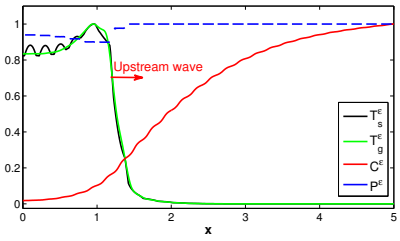

(b) $t = 10$

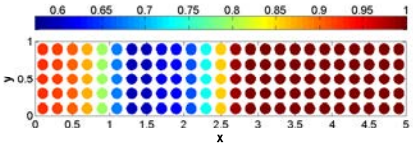

(c) $P^\epsilon, t = 250$

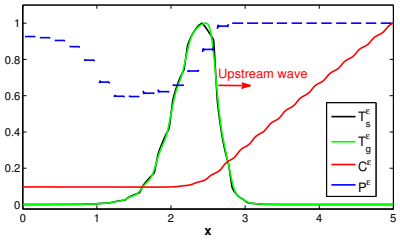

(d) $t = 250$

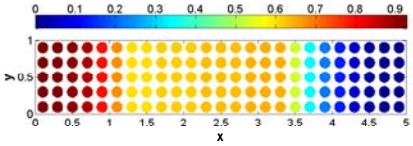

(e) $P^\epsilon, t = 500$

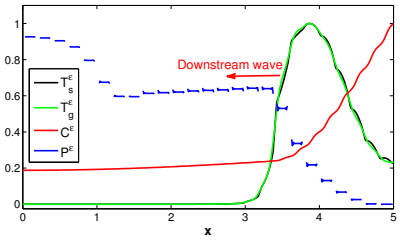

(f) $t = 500$

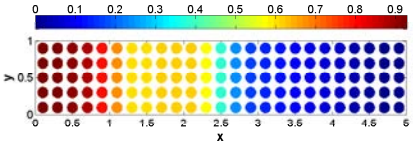

(g) $P^\epsilon, t = 700$

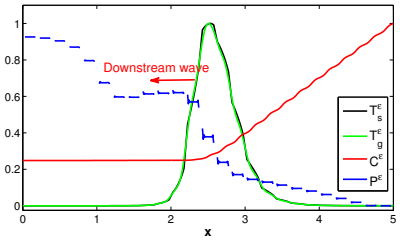

(h) $t = 700$

Figure 5: Evolution of the spatial profiles of solid fuel concentration P^ϵ (a), (c) (respectively (e), (g)) with their corresponding wave structures; (b), (d) upstream smolder waves (respectively (f), (h) downstream smolder waves). The arrows indicate the direction of propagation of the waves.

boundary, the waves reflect downstream and propagate toward the left. The phenomenon of reflecting smolder waves has been observed in microgravity experiment aboard a spacecraft (Olson et al., 1998).

Similar to the case $\sigma = 0$, we simulate the behavior of (20) for the effect of the radiative heat transfer ($\sigma > 0$). We point out that σ essentially controls the intensity of the radiative heat losses to the surroundings. Figure 5 illustrates the evolution of the spatial distribution of P^ϵ at various time instances. The introduction of radiative heat losses results to significant changes the pictures. The spread rate of the wave decreases and hence an increase in the time for the emergence of downstream waves. Also, we notice the leakage of C^ϵ across the front (Figures 5d, 5f and 5h), which intensifies as the waves move downstream. The pattern of the solid fuel shows incomplete conversion of the fuel (Figures 5g and 5h), compared with the complete fuel conversion depicted in Figures 4g and 4h.

3. Asymptotic expansions

In this section, we briefly describe the homogenization procedure for deriving an approximate macroscopic description of the coupled system of equations presented in (20). The starting point of the solution procedure is to assume solutions to system (20) in the form of asymptotic expansions:

$$T^\epsilon(t,x) = T^0(t,x,\frac{x}{\epsilon}) + \epsilon T^1(t,x,\frac{x}{\epsilon}) + \epsilon^2 T^2(t,x,\frac{x}{\epsilon}) + \cdots , \tag{25}$$

$$C^\epsilon(t,x) = C^0(t,x,\frac{x}{\epsilon}) + \epsilon C^1(t,x,\frac{x}{\epsilon}) + \epsilon^2 C^2(t,x,\frac{x}{\epsilon}) + \cdots , \tag{26}$$

$$P^\epsilon(t,x) = P^0(t,x,\frac{x}{\epsilon}) + \epsilon P^1(t,x,\frac{x}{\epsilon}) + \epsilon^2 P^2(t,x,\frac{x}{\epsilon}) + \cdots , \tag{27}$$

where $T^i(t,x,y), C^i(t,x,y)$ and $P^i(t,x,y)$ are assumed to be Y-periodic, with $y = x/\epsilon$. The derivative operator is transformed based on the two spatial variables (x,y) introduced in the problem, i.e.

$$\nabla \mapsto \nabla_x + \frac{1}{\epsilon}\nabla_y. \tag{28}$$

In the next step, we substitute the expansions (25)-(27), using the transformation (28), in (20) and identifying succession of boundary value problems at the same powers of ϵ:

- Equation of order ϵ^{-2} :

$$\begin{cases} -\nabla_y \cdot (\lambda_g \nabla T_g^0) = 0, & \text{in } Y_g, \\ -\nabla_y \cdot (\lambda_s \nabla T_s^0) = 0, & \text{in } Y_s, \\ T_g^0 - T_s^0 = 0, & \text{on } \Gamma, \\ (\lambda_s \nabla_y T_s^0 - \lambda_g \nabla_y T_g^0) \cdot n = 0, & \text{on } \Gamma, \\ \{T_g^0, T_s^0\} \text{ is Y-Periodic.} \end{cases} \tag{29}$$

We deduce that

$$T_g^0(t,x,y) = T_s^0(t,x,y) = T^0(t,x). \tag{30}$$

- Equation of order ϵ^{-1} :

$$\begin{cases} -\nabla_y \cdot (\lambda_g (T_g^1 + \nabla_x T^0)) = 0, & \text{in } Y_g, \\ -\nabla_y \cdot (\lambda_s (T_s^1 + \nabla_x T^0)) = 0, & \text{in } Y_g, \\ T_g^1 - T_s^1 = 0, & \text{on } \Gamma, \\ -(\lambda_g (\nabla_y T_g^1 + \nabla_x T^0) + \lambda_s (\nabla_y T_s^1 + \nabla_x T^0)) \cdot n = 0, & \text{on } \Gamma, \\ \{T_g^1, T_s^1\} \text{ is Y-Periodic.} \end{cases} \tag{31}$$

The linearity of the problem allows to decompose the solution into elementary solutions $\omega_i(y)$ associated with unit macroscopic gradients, i.e. $\nabla_x T^0 = e_i, i = 1, 2$, and satisfying the following so-called cell problems

$$\begin{cases} \dfrac{\partial}{\partial y_j}(\lambda_g(\dfrac{\partial \omega_{gi}}{\partial y_j} + I_{ij})) = 0, & \text{in } Y_g, \\ \dfrac{\partial}{\partial y_j}(\lambda_s(\dfrac{\partial \omega_{si}}{\partial y_j} + I_{ij})) = 0, & \text{in } Y_s, \\ \omega_{gi} - \omega_{si} = 0, & \text{on } \Gamma, \\ (\lambda_s(\dfrac{\partial \omega_{si}}{\partial y_j} + I_{ij}) - \lambda_g(\dfrac{\partial \omega_{gi}}{\partial y_j} + I_{ij})) \cdot n_j = 0, & \text{on } \Gamma, \\ w_i \text{ is Y-Periodic.} \end{cases} \tag{32}$$

The solution, T^1, of (31) is defined by

$$T^1(t,x,y) = \omega(y) \cdot \nabla T^0 + \overline{T}^1(t,x). \tag{33}$$

- Equation of order ϵ^0 :

$$\begin{cases} -\nabla_y\cdot(\lambda_g(\nabla_y T_g^2+\nabla_x T_g^1))-\nabla_x\cdot(\lambda_g(\nabla_y T_g^1+\nabla_x T^0))- \\ \mathcal{C}_{\rm g}\mathbf{u}\cdot\nabla_x T^0+\mathcal{C}_{\rm g}\dfrac{\partial T^0}{\partial t}=0, & \text{in } Y_g, \\ -\nabla_y\cdot(\lambda_s(\nabla_y T_s^2+\nabla_x T_s^1))-\nabla_x\cdot(\lambda_s(\nabla_y T_s^1+\nabla_x T^0))+ \\ \mathcal{C}_{\rm s}\dfrac{\partial T^0}{\partial t}=0, & \text{in } Y_s, \\ T_g^2-T_s^2=0, & \text{on } \Gamma, \\ (\lambda_s(\nabla_y T_s^2+\nabla_x T_s^1)-\lambda_g(\nabla_y T_g^2+\nabla_x T_g^1))\cdot n= \\ Q_1W_1(T^0,C^0,P^0)-\sigma(T^0-T_\infty), & \text{on } \Gamma, \\ \{T_g^2,T_s^2\} \text{ is Y-Periodic.} \end{cases} \tag{34}$$

The existence of a Y-periodic solution implies a compatibility condition which can be established by divergence theorem over Y_g and Y_s. First, we consider the first terms in (34):

$$\int_{Y_g}\nabla_y\cdot(\lambda_g(\nabla_y T_g^2+\nabla_x T_g^1))dY=-\int_\Gamma\lambda_g(\nabla_y T_g^2+\nabla_x T_g^1)\cdot n dS, \tag{35}$$

$$\int_{Y_s}\nabla_y\cdot(\lambda_s(\nabla_y T_s^2+\nabla_x T_s^1))dY=\int_\Gamma\lambda_s(\nabla_y T_s^2+\nabla_x T_s^1)\cdot n dS. \tag{36}$$

The boundary integrals (35)-(36) vanish on the edges of the unit cell Y due to the periodicity of the fluxes and the sign of the integral on the right hand side of (35) changes by taking the outward normal to Y_s. The balance of fluxes on Γ implies that the sum of the integrals is

$$\begin{aligned} \int_\Gamma(\lambda_s(\nabla_y T_s^2+\nabla_x T_s^1)-\lambda_g(\nabla_y T_g^2+\nabla_x T_g^1))\cdot n dS= \\ \int_\Gamma(Q_1W_1(T^0,C^0,P^0)-\sigma\varepsilon(T^0-T_\infty))dS= \\ |\Gamma|Q_1W_1(T^0,C^0,P^0)-|\Gamma|\sigma(T^0-T_\infty). \end{aligned} \tag{37}$$

The second terms of (34) are evaluated by noting that

$$\nabla_y T^1+\nabla_x T^0=(\nabla_y\omega+\mathrm{I})\nabla_x T^0 \tag{38}$$

according to definition (33). It follows, by interchanging the integration

with respect to y and the derivative with respect to x, that

$$\int_Y \nabla_x \cdot (\lambda(\nabla_y T^1 + \nabla_x T^0))dY = \nabla_x \cdot \left((\int_Y \lambda(\nabla_y \omega + \mathrm{I})dY)\nabla_x T^0 \right) \tag{39}$$

The averaging of the remaining terms in (34) is given by

$$\frac{\partial T^0}{\partial t}\left(\int_Y (\mathcal{C}_g + \mathcal{C}_s)dY\right) = c^{\text{eff}}\frac{\partial T^0}{\partial t}, \tag{40}$$

$$\int_Y \mathcal{C}_g \mathbf{u} \cdot \nabla_x T^0 dY = \left(\int_Y \chi_g \mathcal{C}_g \mathbf{u} dY\right) \cdot \nabla_x T^0 = \mathbf{V} \cdot \nabla_x T^0, \tag{41}$$

where $\mathbf{V} = \phi \mathcal{C}_g \mathbf{u}$.

3.1. Macroscopic description

Combining the averages of all terms together, we arrive at the following macroscopic description:

$$\begin{aligned} c^{\text{eff}}\frac{\partial T^0}{\partial t} &= \nabla_x \cdot (\lambda^{\text{eff}} \nabla_x T^0) + \mathbf{V} \cdot \nabla_x T^0 + \\ &|\Gamma| Q_1 W_1(T^0, C^0, P^0) - |\Gamma|\sigma(T^0 - T_\infty), \end{aligned} \tag{42}$$

where

$$\lambda_{ij}^{\text{eff}} = \left(\int_{Y_g} \lambda_g (I_{ij} + \frac{\partial \omega_{gj}}{\partial y_i})dY + \int_{Y_s} \lambda_s (I_{ij} + \frac{\partial \omega_{sj}}{\partial y_i})dY \right), \ i, j = 1, 2. \tag{43}$$

For the homogenization of the concentration, $C^\epsilon(t, x)$, we follow the lead described in Ijioma et al. (2013). We also point out that the final homogenized concentration model is functionally identical, except for the presence of the solid fuel mass concentration.
The homogenized equation for the solid fuel to first order is given by

$$\frac{\partial P^0}{\partial t} = -W_1(T^0, C^0, P^0) + \mathcal{O}(\epsilon). \tag{44}$$

We simply recall the form of the homogenized concentration model, $C^0(t, x)$, (Ijioma et al., 2013), which has the form:

$$\phi \frac{\partial C^0}{\partial t} = \nabla_x \cdot (D^{\text{eff}} \nabla_x C^0) + \tilde{\mathbf{V}} \cdot \nabla_x C^0 - |\Gamma| W_1(T^0, C^0, P^0), \tag{45}$$

where $\tilde{\mathbf{V}} = \phi\mathbf{u}$ with $\mathbf{u} = (V, 0)$ and

$$D_{ij}^{\text{eff}} = D\int_{Y_g}(I_{ij} + \frac{\partial\omega_j}{\partial y_i})dY,\ i,j = 1,2. \tag{46}$$

where, the cell function, ω, given in (46) satisfies the following cell problem for the concentration model:

$$\begin{cases} \dfrac{\partial}{\partial y_j}(D(\dfrac{\partial\omega_i}{\partial y_j} + I_{ij})) = 0, & \text{in } Y_g, \\ (D(\dfrac{\partial\omega_i}{\partial y_j} + I_{ij}))\cdot n_j = 0, & \text{on } \Gamma, \\ w_i \text{ is Y-Periodic.} \end{cases} \tag{47}$$

In (42) and (45), $\phi = |Y_g| / |Y|$ is the system porosity. In a similar notation, we denote the surface porosity given above by $\phi^s = |\Gamma|$.

Remark 3.1. *In practice, the nonlinear reaction rate can be approximated by a step function in the spirit of Turns (2000); Ikeda and Mimura (2008). This follows the introduction of an ignition temperature T_{ign} such that the Arrhenius law can be written in the following form*

$$k(T^0) = \begin{cases} A\exp(-E_1/RT^0), & \text{if } T^0 \geq T_{ign} \\ 0, & 0 < T^0 < T_{ign}, \end{cases} \tag{48}$$

where E_1/R is the activation temperature.

4. Results and discussion

4.1. Numerical study of the efficiency of the homogenization procedure

In the previous sections, we started from a pore scale description, which lead to a homogenization problem. Consequently, a homogenized model was derived with formulas for calculating the effective diffusion coefficients. In this section, we discuss the efficiency of the homogenization procedure. Specifically, we compare the numerical results of the microscopic model with the homogenized model.

It should be noted that convection, chemical reaction and radiative heat transfer do not play dominant roles at the pore scale (cf. (32) for the cell problems and the ϵ-scaling of (20)). We are interested in studying a suitable range for a slow smoldering combustion scenario under microgravity. The convergence study is done by varying ϵ in the microscopic model. Since the

smoldering propagation is essentially one-dimensional, we consider a one-dimensional solution of homogenized equations. However, the microscopic problem is considered in two-dimensions.

In order to minimize computational cost, we impose periodic boundary conditions on the lateral boundaries while we increase the total number of cells along the fixed length L_1. We assume that the length $L_2 = \mathcal{O}(\epsilon)$ for each varying ϵ and hence the problem is quasi-one-dimensional. In the numerical experiments, the values of ϵ satisfy $\epsilon \leq \epsilon_f < 0$, i.e., ϵ is considered to be moderately small and ϵ_f is its final value used in the numerical experiments.

In each numerical experiment, we run the simulation by varying the characteristic size of the Y-cell. We begin with cells of characteristic size $l = 2.5$, which corresponds in this case to $\epsilon = 0.5$. Then, we decrease l in each subsequent simulation until the last experiment corresponding to ϵ_f. The time step of the simulations is $dt = 10$. For the computation of the homogenized model, we follow the general homogenization procedure for periodic structures:

1. Solve the corresponding cell problems (32) and (47) of the field variables T^0 and C^0, in each of the canonical directions, $e_j, j = 1, 2$.

2. Calculate the effective thermal conductivity, λ^{eff}, and mass diffusivity, D^{eff}, coefficients using the solutions of their corresponding cell problems

3. Solve the coupled system of homogenized equations for T^0, C^0 and P^0.

For the computations of the cell problems and the homogenized equations, we use the parameter values given in Table 1. The error, ERR, in the approximation is evaluated in the $L^2(0, \tau; \Omega)$ norm, i.e.,

$$ERR_i = \|\psi^\epsilon - \psi^0\|_{L^2(0,\tau_i;\Omega)}, \ i = 1, \cdots, N_t, \tag{49}$$

where i represents the error after a given number of time steps τ_i and N_t, is an integer corresponding to the final time step. This is done to study the evolution of the error for various values of τ due to the transient nature of the problem.

4.2. Upstream waves

We consider a situation, in which the waves only move upstream, i.e., from left to right. In order to achieve this behavior, we suitably choose parameters of the convective transport. As mentioned in Ijioma et al. (2013),

Parameters	Values	Description
r	0.4	Radius of solid fuel cell
$\phi = 1 - \pi r^2$	0.497	Porosity
$\phi^s = 2\pi r$	2.513	Tortuosity
λ_g	$2.38 \cdot 10^{-4}$	Thermal conductivity of gas
λ_s	$7.0 \cdot 10^{-4}$	Thermal conductivity of solid
D	0.25	Molecular diffusion
$\mathcal{C}_g$	1.571×10^{-3}	Heat capacity of gas
$\mathcal{C}_s$	0.6858	Heat capacity of solid
λ^{eff}	3.9562×10^{-4}	Effective thermal conductivity
D^{eff}	0.080523	Effective mass diffusivity
c^{eff}	0.345502	Effective heat capacity

Table 1: Parameter values used in the numerical simulations.

ϵ	0.5	0.3333	0.1	0.0833
ERR_1	2.3769e-02	1.3544e-02	3.8069e-03	3.4309e-03
ERR_2	6.5105e-02	4.6715e-02	3.9731e-02	1.6735e-02
ERR_3	1.1273e-01	9.2423e-02	8.5266e-02	3.3949e-02

Table 2: Evolution of the error in the temperature at various time steps and ϵ .

the parameter A in the Arrhenius kinetics enhances convective transport. When A is relatively small, for example, $A = 0.01$, the waves move momentarily upstream and downstream smolder wave is not viable. Figure 6 show qualitative comparison of results between the full microscopic problem (system size, $L_1 = 5, L_2 = 1$, consists of 125 cells for $\epsilon = 0.2$) with the homogenized problem. In Figures 7, 8 and 9 we show the behavior of the solutions between the microscopic and the homogenized models for varying ϵ. As we can seen, the microscopic solutions become closer to the homogenized solution as ϵ decreases.

ϵ	0.5	0.3333	0.1	0.0833
ERR_1	1.1944e-03	8.9172e-04	5.8676e-04	5.5292e-04
ERR_2	3.5618e-03	2.5880e-03	2.0027e-03	7.2743e-04
ERR_3	5.4323e-03	4.6473e-03	3.9891e-03	1.2992e-03

Table 3: Evolution of the error in the oxidizer concentration at various time steps and ϵ.

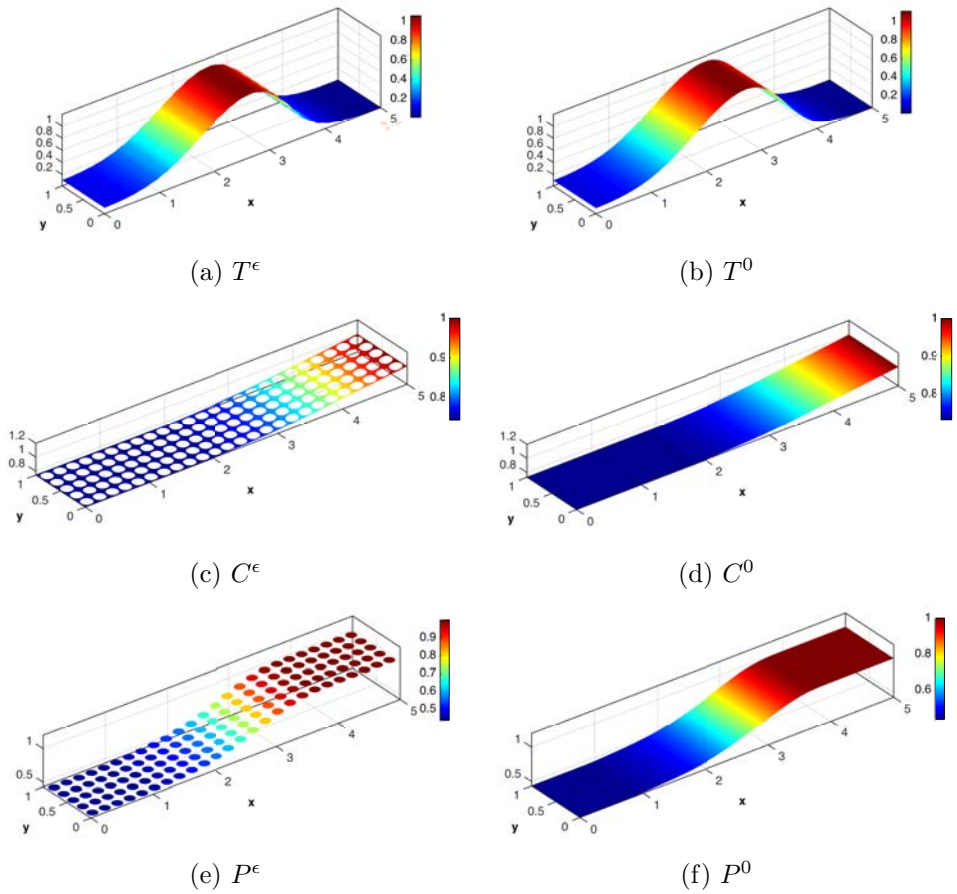

(a) T^ϵ (b) T^0

(c) C^ϵ (d) C^0

(e) P^ϵ (f) P^0

Figure 6: Comparison between the microscopic solutions T^ϵ, C^ϵ and P^ϵ and the homogenized solutions T^0, C^0 and P^0 at $\tau = 2000$ and for $\epsilon = 0.2$. The parameter values are similar to those used in Figure 7.

ϵ	0.5	0.3333	0.1	0.0833
ERR_1	2.5226e-02	1.6815e-02	5.1671e-03	4.2526e-03
ERR_2	3.9322e-02	2.6225e-02	9.6611e-03	7.5167e-03
ERR_3	4.4894e-02	3.1098e-02	1.8966e-02	9.9960e-03

Table 4: Evolution of the error in the solid fuel concentration at various time steps and ϵ.

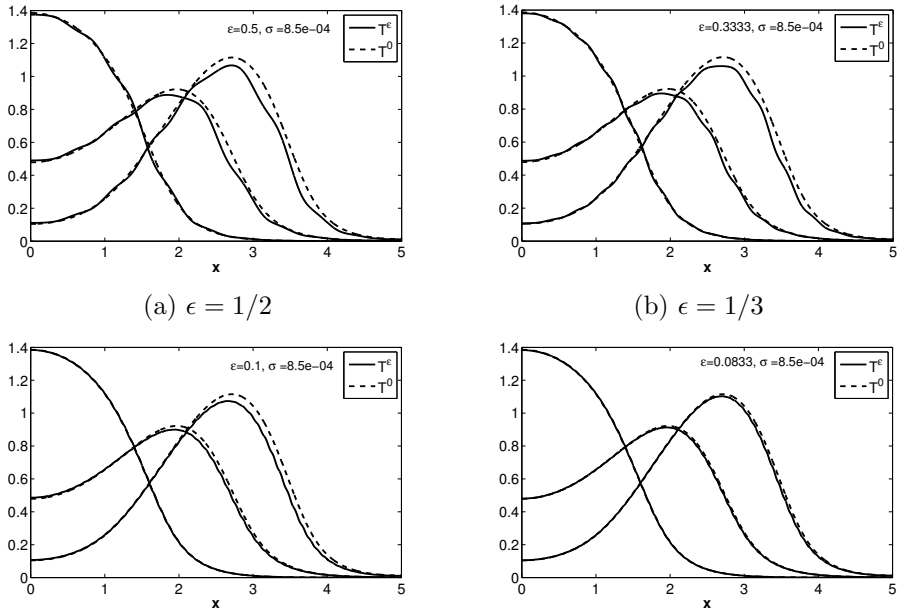

(a) $\epsilon = 1/2$ (b) $\epsilon = 1/3$

(c) $\epsilon = 1/10$ (d) $\epsilon = 1/12$

Figure 7: Comparison between the homogenized and microscopic solutions for varying ϵ in the temperature distribution at various instants of time: (1) $\tau_1 = 500$; (2) $\tau_2 = 1000$; (3) $\tau_3 = 2000$; ($\sigma = 8.5 \times 10^{-4}, T_a = 1.0, A = 0.01, Q = 2.5, V = 0.001$.)

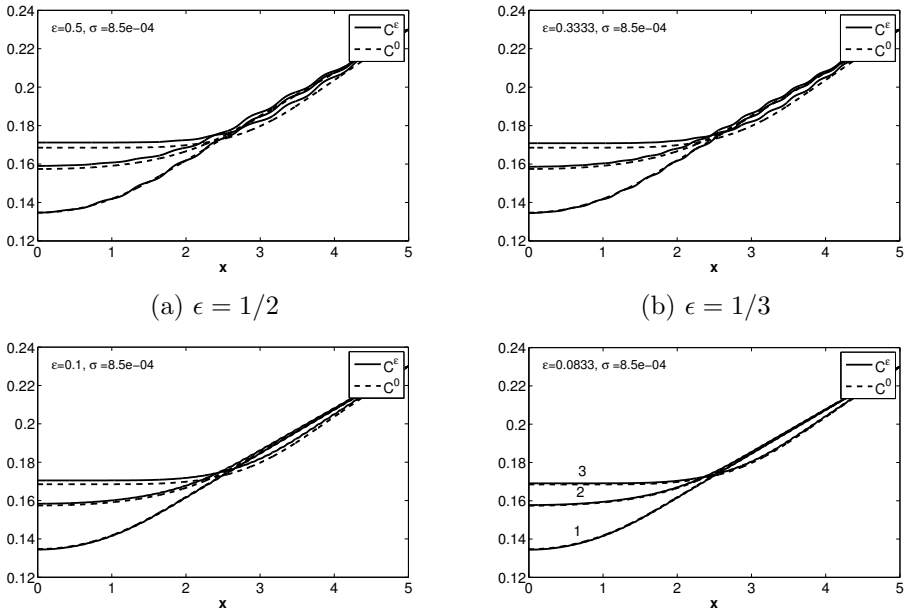

(a) $\epsilon = 1/2$ (b) $\epsilon = 1/3$

(c) $\epsilon = 1/10$ (d) $\epsilon = 1/12$

Figure 8: Comparison between the homogenized and microscopic solutions for varying ϵ in the oxygen concentration distribution at various instants of time: (1) $\tau_1 = 500$; (2) $\tau_2 = 1000$; (3) $\tau_3 = 2000$; ($\sigma = 8.5 \times 10^{-4}, T_a = 1.0, A = 0.01, Q = 2.5, V = 0.001$.)

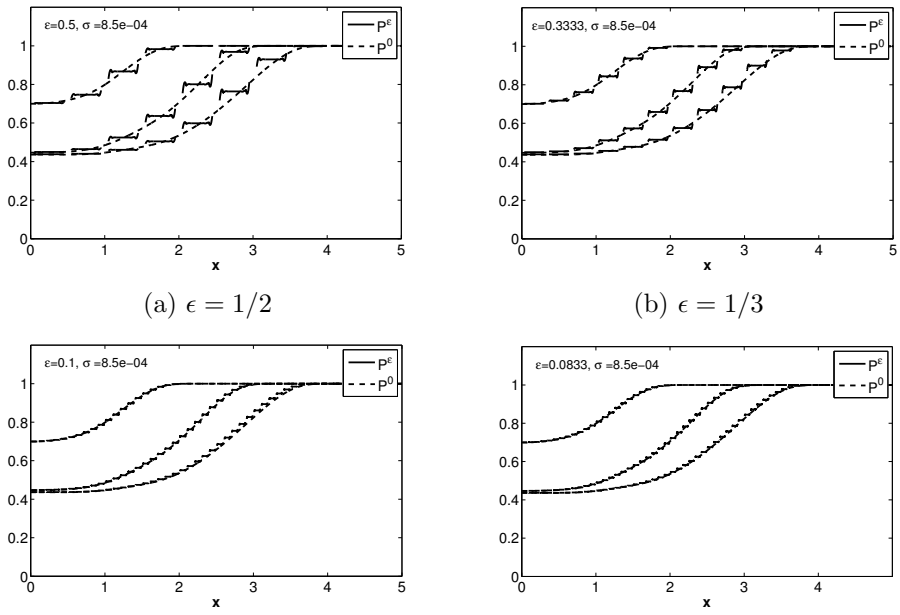

(a) $\epsilon = 1/2$ (b) $\epsilon = 1/3$

(c) $\epsilon = 1/10$ (d) $\epsilon = 1/12$

Figure 9: Comparison between the homogenized and microscopic solutions for varying ϵ in the solid fuel concentration distribution at various instants of time: (1) $\tau_1 = 500$; (2) $\tau_2 = 1000$; (3) $\tau_3 = 2000$; ($\sigma = 8.5 \times 10^{-4}, T_a = 1.0, A = 0.01, Q = 2.5, V = 0.001$.)

The convergence rate at various time steps is also shown in Tables 2, 3 and 4. The results show that, for each value of ϵ, the error increases as the waves approach the right boundary. The explanation for this behavior is simply due to the transient nature of the problem towards the boundaries. However, for each τ_i the errors decrease as ϵ becomes smaller.

4.3. The limit problem $T_a \to 0$

We consider the problem when T_a tends to zero. Hence, we obtain formally a reaction rate of the form

$$W(C^0, P^0) = AC^0P^0. \tag{50}$$

(50) simplifies the nonlinear behavior of the problem. The limit problem (i.e., $T_a \to 0$) suffices for the numerical test for convergence, which is performed based on the assumption that the smoldering propagation is essentially one-dimensional. However, this simplification may impose some limitations on the mechanism of the smoldering combustion process in higher dimensions. Figure 10 depicts a qualitative comparison between the full microscopic problem, consisting of 125 cells for $\epsilon = 0.2$, with the homogenized problem. Here, we consider only the waves moving downstream from the right end of the domain. As can be seen, the solutions at the two descriptions show good qualitative agreement. In Figure 11, 12 and 13, we see that the microscopic solutions are much closer to the solution of the homogenized problem when we decrease ϵ up to a final value $\epsilon_f = 0.05$. Their corresponding differences in the L^2-norm are given in Tables 5, 6 and 7.

ϵ	ERR_1	ERR_2	ERR_3	ERR_4
0.5	4.4607e-01	2.5062e-01	2.2349e-01	2.1847e-01
0.3333	2.1481e-01	1.6495e-01	1.4392e-01	1.2758e-01
0.2	9.5693e-02	7.0833e-02	6.3393e-02	5.8815e-02
0.1	3.7748e-02	3.4025e-02	3.2574e-02	3.3360e-02
0.0833	3.2100e-02	2.5135e-02	3.0492e-02	3.0842e-02
0.05	1.8580e-02	2.2144e-02	2.0524e-02	2.4350e-02

Table 5: Evolution of the error in the distribution of temperature at various time steps and ϵ.

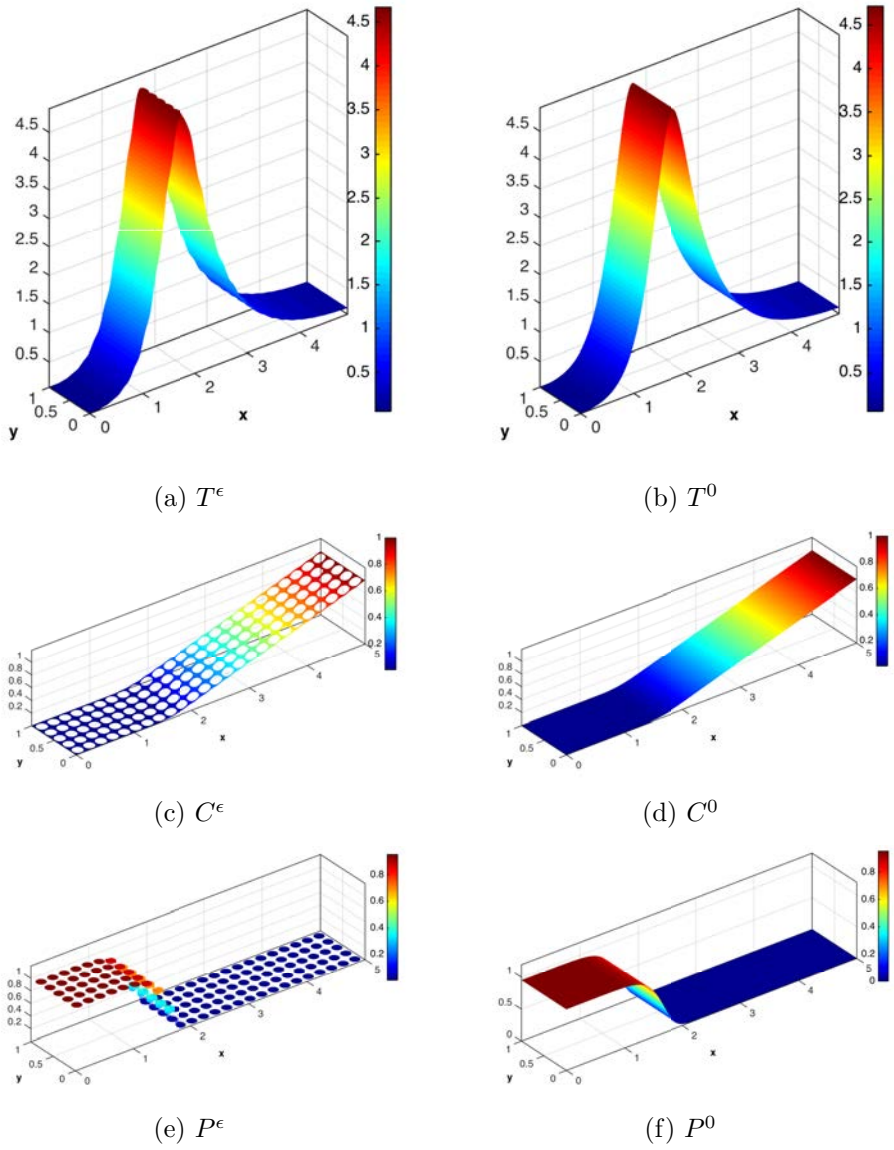

(a) T^ϵ (b) T^0

(c) C^ϵ (d) C^0

(e) P^ϵ (f) P^0

Figure 10: Comparison between the microscopic solutions T^ϵ, C^ϵ and P^ϵ and the homogenized solutions T^0, C^0 and P^0 at $\tau = 750$ and for $\epsilon = 0.2$. The parameter values are similar to those used in Figure 11.

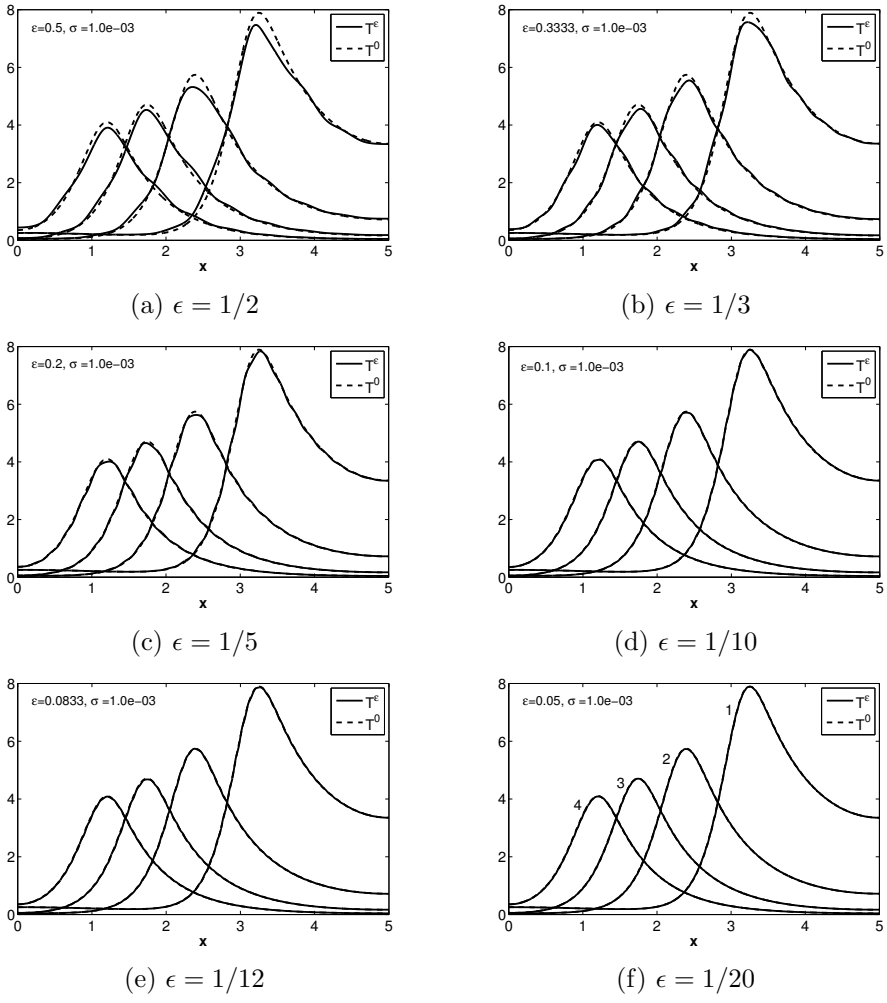

(a) $\epsilon = 1/2$ (b) $\epsilon = 1/3$

(c) $\epsilon = 1/5$ (d) $\epsilon = 1/10$

(e) $\epsilon = 1/12$ (f) $\epsilon = 1/20$

Figure 11: Comparison between the homogenized and microscopic solutions for varying ϵ in the temperature distribution at various instants of time: (1) $\tau_1 = 250$; (2) $\tau_2 = 500$; (3) $\tau_3 = 750$; (4) $\tau_4 = 1000$; ($\sigma = 1.0 \times 10^{-3}, T_a = 0.0, A = 1.5, Q = 2.5, V = 0.001$). In this case, the waves propagate from right to left.

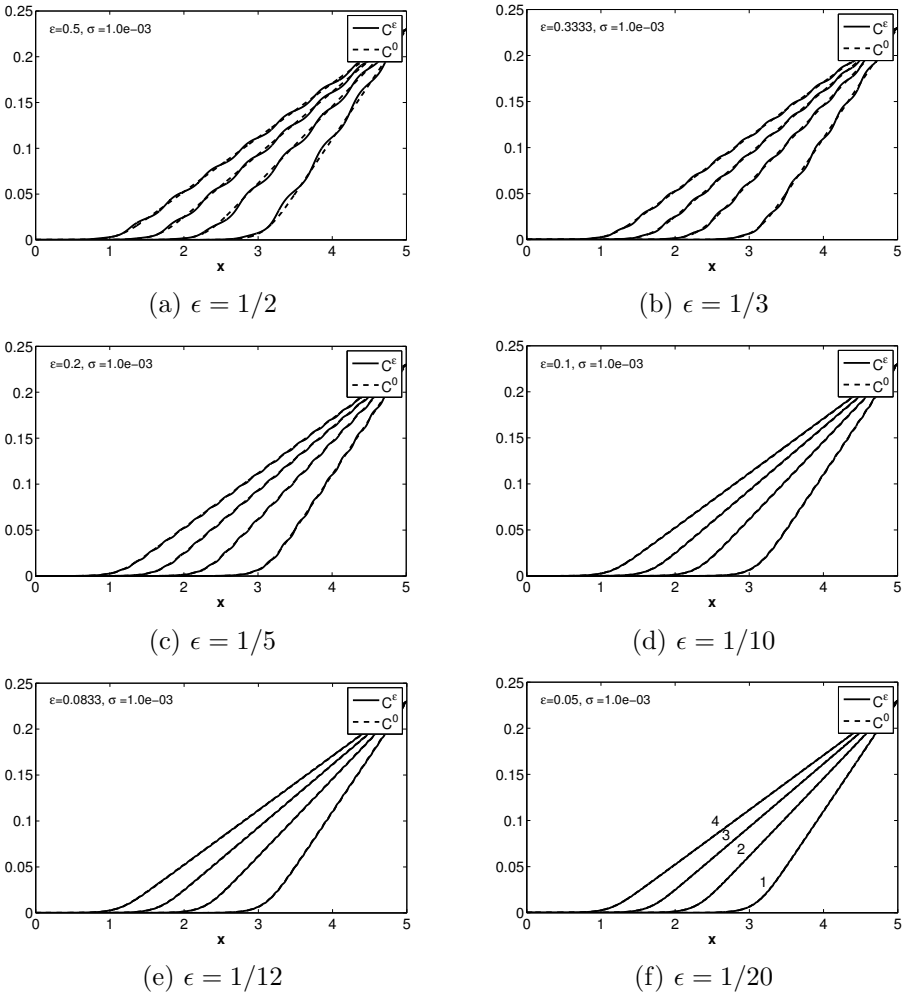

(a) $\epsilon = 1/2$ (b) $\epsilon = 1/3$

(c) $\epsilon = 1/5$ (d) $\epsilon = 1/10$

(e) $\epsilon = 1/12$ (f) $\epsilon = 1/20$

Figure 12: Comparison between the homogenized and microscopic solutions for varying ϵ in the oxygen concentration distribution at various instants of time: (1) $\tau_1 = 250$; (2) $\tau_2 = 500$; (3) $\tau_3 = 750$; (4) $\tau_4 = 1000$; ($\sigma = 1.0 \times 10^{-3}, T_a = 0.0, A = 1.5, Q = 2.5, V = 0.001$).

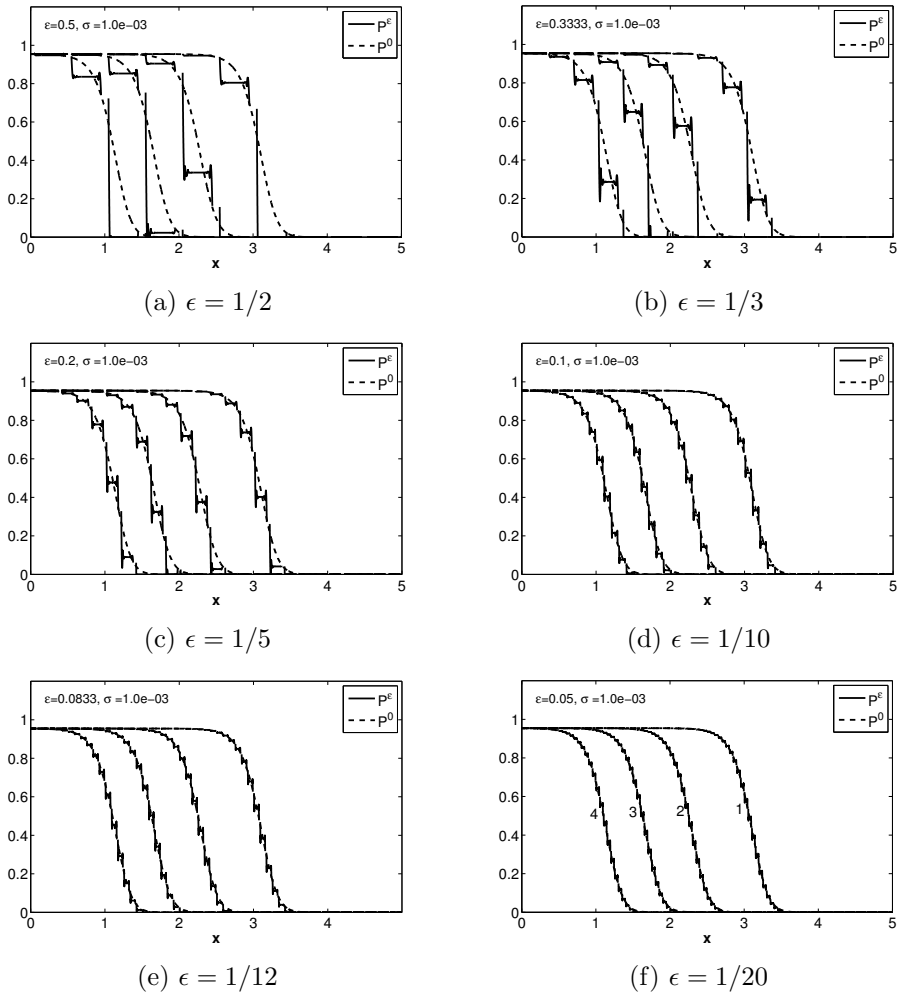

(a) $\epsilon = 1/2$ (b) $\epsilon = 1/3$

(c) $\epsilon = 1/5$ (d) $\epsilon = 1/10$

(e) $\epsilon = 1/12$ (f) $\epsilon = 1/20$

Figure 13: Comparison between the homogenized and microscopic solutions for varying ϵ in the soil fuel concentration distribution at various instants of time: (1) $\tau_1 = 250$; (2) $\tau_2 = 500$; (3) $\tau_3 = 750$; (4) $\tau_4 = 1000$; ($\sigma = 1.0 \times 10^{-3}, T_a = 0.0, A = 1.5, Q = 2.5, V = 0.001$). In this case, the waves propagate from right to left.

ϵ	ERR_1	ERR_2	ERR_3	ERR_4
0.5	5.4533e-03	4.3040e-03	3.4725e-03	3.1391e-03
0.3333	2.9106e-03	2.4108e-03	2.2085e-03	2.0515e-03
0.2	1.7084e-03	1.4633e-03	1.3887e-03	1.3465e-03
0.1	8.6454e-04	8.0037e-04	8.1500e-04	7.3192e-04
0.0833	7.2025e-04	6.1495e-04	6.8190e-04	6.4356e-04
0.05	4.4386e-04	4.8038e-04	5.5041e-04	6.1379e-04

Table 6: Evolution of the error in the distribution of oxygen concentration at various time steps and ϵ.

ϵ	ERR_1	ERR_2	ERR_3	ERR_4
0.5	1.6715e-01	1.5334e-01	2.0088e-01	1.8989e-01
0.3333	1.0153e-01	9.7010e-02	1.0784e-01	9.1725e-02
0.2	5.6730e-02	5.6486e-02	5.6651e-02	5.3134e-02
0.1	2.5237e-02	2.4682e-02	2.4607e-02	2.4617e-02
0.0833	2.0743e-02	2.0778e-02	2.0223e-02	2.0042e-02
0.05	1.1848e-02	1.1743e-02	1.2051e-02	1.2310e-02

Table 7: Evolution of the error in the distribution of solid fuel concentration at various time steps and ϵ.

4.4. Upstream and downstream waves

As we illustrated numerically in Figures 4 and 5, the proposed model has the feature of exhibiting both upstream and downstream waves if the parameter values are within a suitable range. We show that the results of the homogenization procedure are consistent with the predictions of the microscopic model. We run simulations by varying the size of ϵ in the microscopic model in each run. In this case, the value of the intensity of the radiative heat loss is fixed, e.g., $\sigma = 1.0 \times 10^{-2}$. We consider a final time step $\tau = 600$ when the waves reach an intermediate point in the spatial domain after reflecting downstream.

Figures 14, 15 and 16 depict comparison between the homogenized and microscopic solutions for varying ϵ in the distribution of the temperature, oxygen concentration and solid fuel mass concentration respectively. The pictures consist of various time instants at which the error between the homogenized and microscopic solutions of the upstream and downstream waves are compared. It can be seen that the results show good agreement between

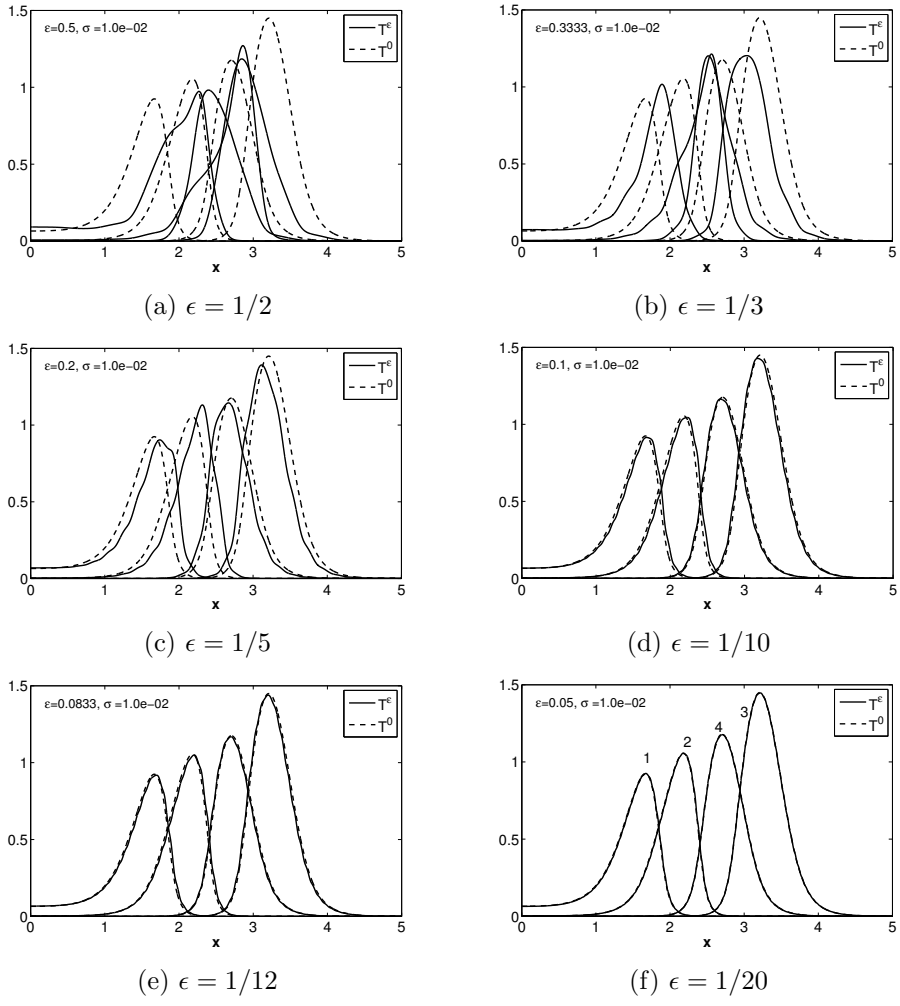

(a) $\epsilon = 1/2$ (b) $\epsilon = 1/3$

(c) $\epsilon = 1/5$ (d) $\epsilon = 1/10$

(e) $\epsilon = 1/12$ (f) $\epsilon = 1/20$

Figure 14: Comparison between the homogenized and microscopic solutions for varying ϵ in the temperature distribution at various instants of time: (1), (2) upstream waves at $\tau_1 = 50, \tau_2 = 100$; (3), (4) downstream waves at $\tau_3 = 400, \tau_4 = 500$. The parameter values used in the simulation include: $\sigma = 1.0 \times 10^{-2}, T_a = 1.0, A = 1.5, Q = 2.5, V = 0.001$.

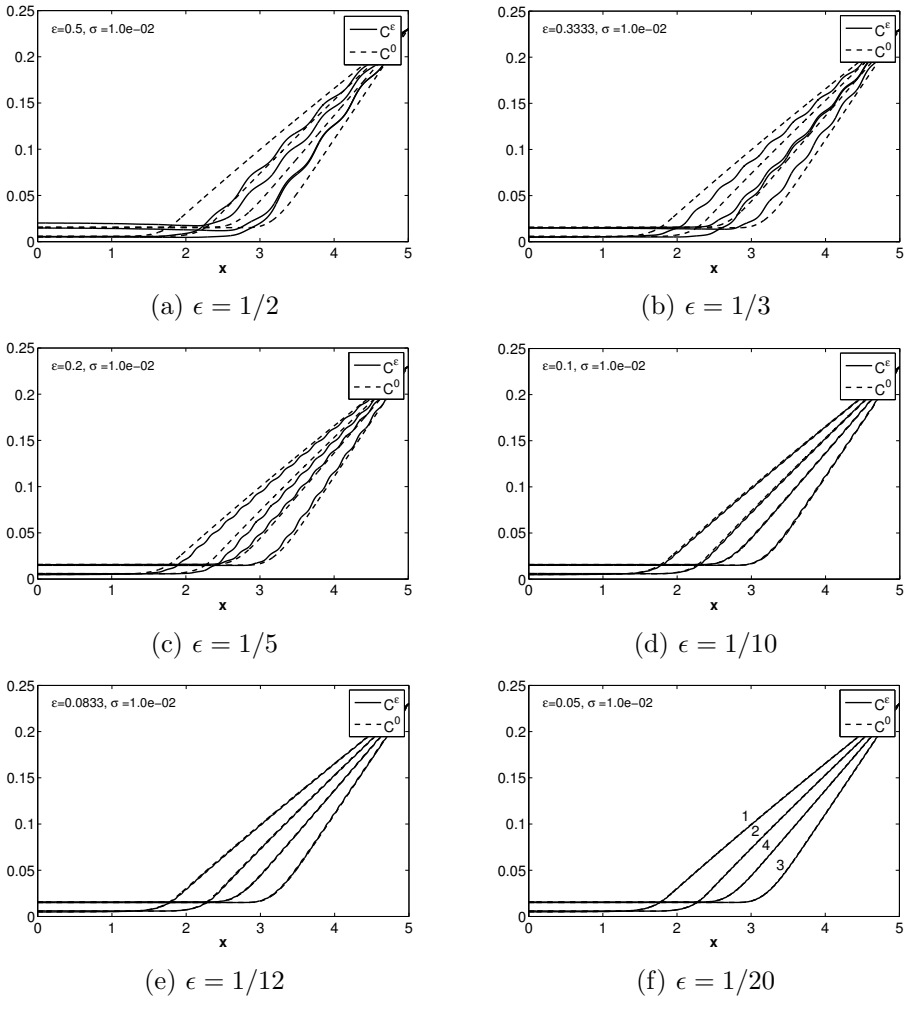

(a) $\epsilon = 1/2$ (b) $\epsilon = 1/3$

(c) $\epsilon = 1/5$ (d) $\epsilon = 1/10$

(e) $\epsilon = 1/12$ (f) $\epsilon = 1/20$

Figure 15: Comparison between the homogenized and microscopic solutions for varying ϵ in the oxidizer concentration distribution at various instants of time: (1), (2) upstream waves at $\tau_1 = 50, \tau_2 = 100$; (3), (4) downstream waves at $\tau_3 = 400, \tau_4 = 500$. The parameter values used in the simulation include: $\sigma = 1.0 \times 10^{-2}, T_a = 1.0, A = 1.5, Q = 2.5, V = 0.001$.

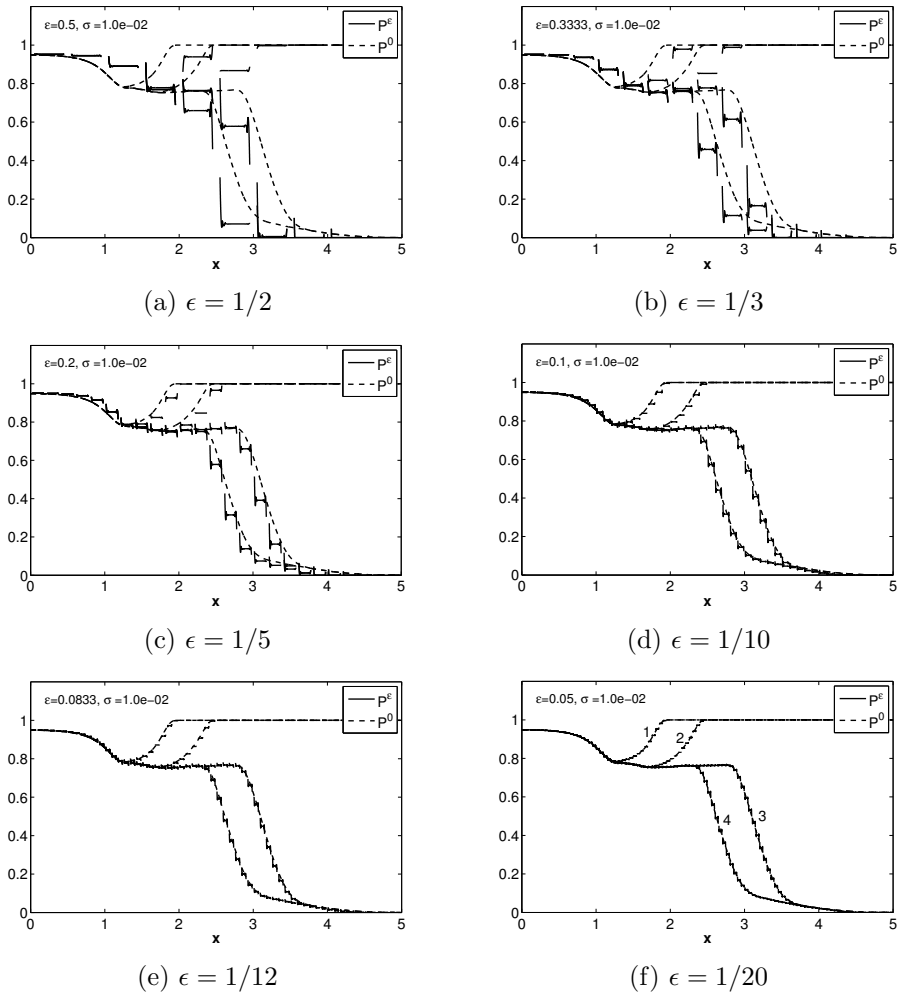

(a) $\epsilon = 1/2$ (b) $\epsilon = 1/3$

(c) $\epsilon = 1/5$ (d) $\epsilon = 1/10$

(e) $\epsilon = 1/12$ (f) $\epsilon = 1/20$

Figure 16: Comparison between the homogenized and microscopic solutions for varying ϵ in the solid fuel concentration distribution at various instants of time: (1), (2) upstream waves at $\tau_1 = 50, \tau_2 = 100$; (3), (4) downstream waves at $\tau_3 = 400, \tau_4 = 500$. The parameter values used in the simulation include: $\sigma = 1.0 \times 10^{-2}, T_a = 1.0, A = 1.5, Q = 2.5, V = 0.001$.

the homogenized solution and the microscopic solution as ϵ decreases; specifically at $\epsilon = 0.05$.

ϵ	ERR_1	ERR_2	ERR_3	ERR_4
0.5	6.6289e-01	8.7065e-01	7.4827e-01	4.9378e-01
0.3333	4.4293e-01	6.6538e-01	4.9992e-01	3.8446e-01
0.2	2.3549e-01	2.9268e-01	2.2455e-02	1.4456e-02
0.1	5.9462e-02	7.1919e-02	5.3495e-02	3.5008e-02
0.0833	3.5832e-02	4.1790e-02	3.9806e-02	2.6262e-02
0.05	1.2216e-02	1.1548e-02	5.9865e-02	7.0734e-02

Table 8: Evolution of the error in the distribution of temperature at various time steps and ϵ.

ϵ	ERR_1	ERR_2	ERR_3	ERR_4
0.5	3.2599e-02	5.5355e-02	2.2256e-02	1.9343e-02
0.3333	1.9194e-02	2.9978e-02	1.4742e-02	1.1485e-02
0.2	9.8237e-03	1.1136e-02	6.3736e-03	4.7070e-03
0.1	2.5306e-03	2.5794e-03	1.5661e-03	1.1813e-03
0.0833	1.5309e-03	1.4222e-03	1.3034e-03	9.6558e-04
0.05	7.9532e-04	7.0263e-04	4.5529e-04	4.6887e-04

Table 9: Evolution of the error in the distribution of oxygen concentration at various time steps and ϵ.

ϵ	ERR_1	ERR_2	ERR_3	ERR_4
0.5	1.1917e-01	1.4484e-01	2.4931e-01	2.1805e-01
0.3333	8.6752e-02	9.9117e-02	1.6843e-01	1.4442e-01
0.2	4.1161e-02	4.6729e-02	7.6613e-02	6.6338e-02
0.1	1.2805e-02	1.4095e-02	2.4684e-02	2.2698e-02
0.0833	9.1683e-03	9.5601e-03	1.9109e-02	1.7636e-02
0.05	4.2196e-03	4.3521e-03	9.5951e-03	9.3808e-03

Table 10: Evolution of the error in the distribution of solid fuel concentration at various time steps and ϵ.

4.5. Effect of the radiative heat losses

One of the features of the models derived in this study is the incorporation of the influence of radiative heat losses. We recall that our assumptions

wave	$\sigma = 0.0$	$\sigma = 8 \times 10^{-4}$	$\sigma = 2 \times 10^{-3}$	$\sigma = 2 \times 10^{-2}$
upstream	2.8421e-02	9.2658e-02	3.0416e-02	1.5294e-02
downstream	3.6042e-02	3.1050e-02	2.9316e-02	4.3259e-02

Table 11: Comparison of error in the distribution of temperature between the homogenized and microscopic model at various σ and for $\epsilon = 0.05$.

on the microscopic model demand that radiative effects do not play dominant roles at the pore scale. However, we examine the effect of the intensity of radiative heat loss, σ, on the efficiency of the homogenization process. Thus, we run simulations for various values of σ. For brevity of presentation, we fix $\epsilon = 0.05$, which serves, for the convergence tests in the previous sections, as the final value of ϵ. Figure 17 shows the distributions of temperature, oxygen concentration and solid fuel mass concentration at $\sigma = 0.0$ (profile 1), $\sigma = 8 \times 10^{-4}$ (profile 2), $\sigma = 2 \times 10^{-3}$ (profile 3), $\sigma = 2 \times 10^{-2}$ (profile 4). At lower values of σ ($\sigma = 0, 8 \times 10^{-4}, 2 \times 10^{-3}$), the extent of propagation of the waves in the spatial domain, in both upstream and downstream regimes, is larger compared with when $\sigma = 2 \times 10^{-2}$ (profile 4). Thus, the spread rate of the waves decreases at higher values of σ, which is consistent with previous microgravity experiments (see Fakheri and Olson, 1989, e.g.). Figure 17a (profile 4) indicates an abrupt drop in the temperature distribution behind the front. Increasing σ beyond this value may lead to the extinction of the combustion process. The effect of radiative heat losses in combustion have been notably studied in the literature (see Kagan and Sivashinsky, 1996, 1997, e.g.) as well as its role in microgravity smoldering combustion experiments (Zik and Moses, 1999; Fakheri and Olson, 1989, e.g.). It is known, at sufficiently high heat losses, that the range of thermal-diffusive instability of the smolder waves is enhanced (Kagan and Sivashinsky, 1997), which usually involves the leakage of reactants through the front. The latter is depicted in Figure 17c, 17d and 17f (profile 4); the solid fuel and oxygen are not completely consumed by the chemical reaction.

Concerning the errors between the homogenized and microscopic models, we see that the errors attain maximum values for the downstream waves at $\sigma = 2.0 \times 10^{-2}$ (Tables 11, 12 and 13 (downstream)). In all cases, the error increases as radiation becomes dominant at the pore level, except for the upstream temperature distribution, which indicates a decrease in the error.

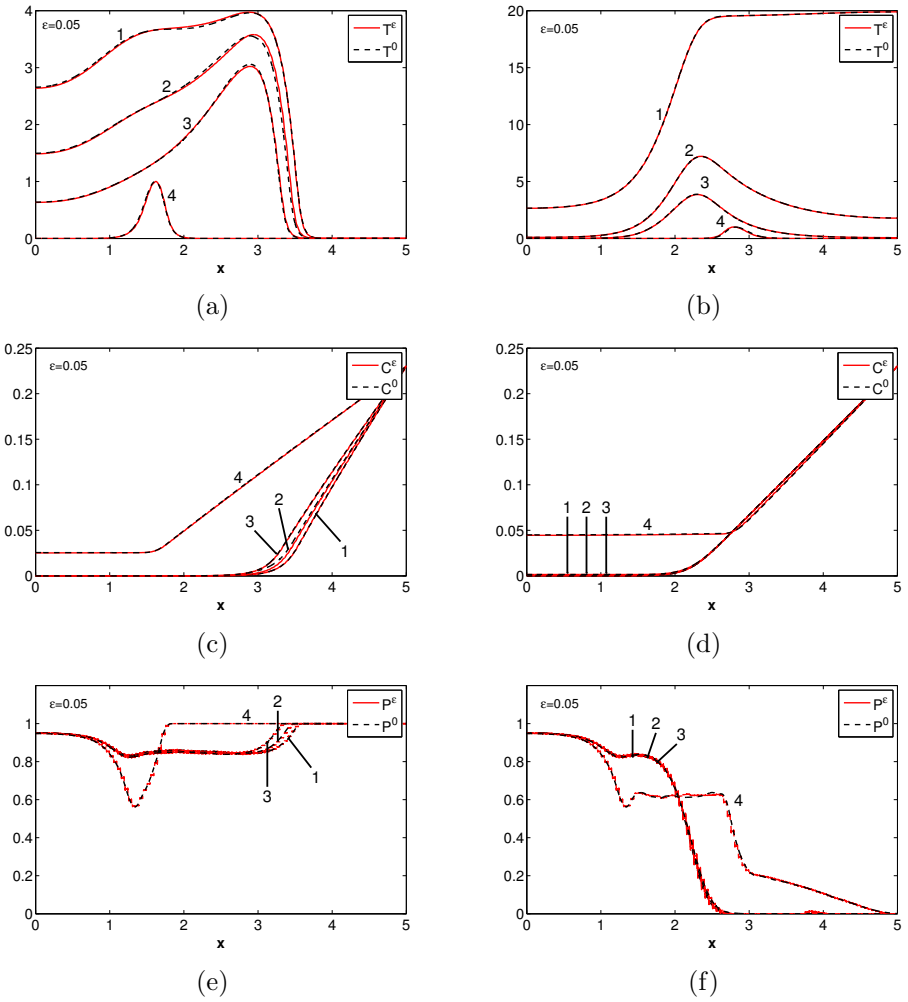

Figure 17: Comparison between the homogenized solution and microscopic solution ($\epsilon = 0.05$) for varying σ in the distribution of (a), (b) temperature; (c), (d) oxygen concentration; (e), (f) solid fuel concentration, at two instants of time corresponding to (a), (c) and (e) upstream waves at $\tau = 100$; (b), (d) and (f) downstream waves at $\tau = 600$. The parameter values used in the simulation include: $T_a = 1.0, A = 1.5, Q = 2.5, V = 0.001$ and $\sigma = 0.0$ (1), $\sigma = 8.0 \times 10^{-4}$ (2), $\sigma = 2.0 \times 10^{-3}$ (3), $\sigma = 2.0 \times 10^{-2}$ (4).

wave	$\sigma = 0.0$	$\sigma = 8 \times 10^{-4}$	$\sigma = 2 \times 10^{-3}$	$\sigma = 2 \times 10^{-2}$
upstream	4.6202e-04	3.5264e-03	8.4037e-04	9.8141e-04
downstream	4.6257e-04	4.8245e-04	6.4897e-04	1.3293e-03

Table 12: Comparison of error in the distribution of oxygen concentration between the homogenized and microscopic model at various σ and for $\epsilon = 0.05$.

wave	$\sigma = 0.0$	$\sigma = 8 \times 10^{-4}$	$\sigma = 2 \times 10^{-3}$	$\sigma = 2 \times 10^{-2}$
upstream	4.2644e-03	6.3927e-03	4.5155e-03	1.0233e-02
downstream	1.1533e-02	1.0568e-02	9.8950e-03	1.6408e-02

Table 13: Comparison of error in the distribution of solid fuel mass concentration between the homogenized and microscopic model at various σ and for $\epsilon = 0.05$.

4.6. Two-dimensional fingering instability

In order to illustrate the behavior of the macroscopic model for a problem of microgravity reverse smoldering combustion, we perform numerical simulations on a dimensionless version of the macroscopic model (see (42), (44) and (45)). We scale the model as detailed in Fasano et al. (2009) so that the following reference quantities are considered:

$$u = \frac{T^0}{T_b}, v = \frac{C^0}{C_0}, w = \frac{P^0}{P_0}, (\tilde{x}, \tilde{y}) = \frac{(x, y)}{L}, t^* = \frac{t}{t_D}, \tag{51}$$

$$\begin{aligned} u_t &= \frac{\lambda^{\text{eff}}}{D^{\text{eff}} c^{\text{eff}}} \triangle u + \frac{\mathcal{C}_{\text{g}}}{c^{\text{eff}}} \phi \frac{VL}{D^{\text{eff}}} u_x + \phi^s \frac{t_D Q_1 C_0}{c^{\text{eff}} T_b} f(u, v, w) - \phi^s \frac{t_D \sigma}{c^{\text{eff}}} (u - \tilde{u}), \\ \phi v_t &= \triangle v + \phi \frac{VL}{D^{\text{eff}}} v_x - \phi^s t_D f(u, v, w), \\ w_t &= -t_D H_w f(u, v, w) \end{aligned}$$

and the dimensionless system of equations reduces to

$$\begin{aligned} u_t &= Le \triangle u + \phi \Lambda Pe u_x + \beta \gamma f(u, v, w) - a(u - \tilde{u}), \\ \phi v_t &= \triangle v + \phi Pe v_x - \gamma f(u, v, w), \\ w_t &= -H_w \gamma f(u, v, w), \end{aligned} \tag{52}$$

where

$$Le = \frac{\lambda^{\text{eff}}}{D^{\text{eff}} c^{\text{eff}}}, Pe = \frac{VL}{D^{\text{eff}}}, \Lambda = \frac{\mathcal{C}_{\text{g}}}{c^{\text{eff}}}, \beta = \frac{Q_1 C_0}{c^{\text{eff}} T_b}, \tag{53}$$

$$t_D = \frac{L^2}{D^{\text{eff}}}, \gamma = \phi^s t_D A, a = \frac{\phi^s t_D \sigma}{c^{\text{eff}}}, H_w = \frac{C_0}{\phi^s P_0}. \tag{54}$$

The consumption rate of the reactants is given by the following Arrhenius law:

$$f(u,v,w) = \begin{cases} vw\exp(-\theta/u), & \text{if } u \geq u^* \\ 0, & \text{otherwise.} \end{cases} \tag{55}$$

where $T_b = T_\infty + Q_1 C_0/c^{\text{eff}}$ is the adiabatic temperature of combustion products; $\theta = E_1/RT_b$ is the dimensionless activation temperature; $\tilde{u} = T_\infty/T_b \ll 1$ is the dimensionless temperature of the surroundings and u^* is the dimensionless ignition temperature.

Remark 4.1. *It should be pointed out that for most phenomenological models (cf. Ikeda and Mimura (2008)) that neglect the contribution of the presence of obstacles, the system porosity, ϕ, in* (52) *may be set equal to unity. However, for such an approximation, the essential physics of the phenomena of interest is still viable.*

We consider the problem (52) with (55) in a bounded rectangular domain $0 < x < L_x, 0 < y < L_y$ ($L_x = 400, L_y = 200$), in which the lateral walls are subjected to Neumann conditions:

$$u_y = v_y = 0 \ \text{ at } y = 0, L_y.$$

At the inlet end (i.e., $x = L_x$) and the outlet end (i.e., $x = 0$), the following conditions are prescribed for the field variables u and v:

$$(u_x, v_x)(t,0,y) = (0,0), (u_x, v)(t, L_x, y) = (0, v_0), \quad t > 0. \tag{56}$$

The boundary descriptions (56) imply that ignition is initiated at the left boundary and the combustion fronts propagate from the left to the right boundary, thus setting up a reverse combustion. This configuration is known to exert a destabilizing effect on the emerging combustion fronts (Zik and Moses, 1999; Olson et al., 1998). Finally, the system (52) is closed by the following initial conditions:

$$u(0,x,y) = \begin{cases} 2 + \varepsilon(y), & \text{if } 0 \leq x \leq 5 + \varepsilon(y), 0 \leq y \leq L_y, \\ \tilde{u}, & \text{otherwise,} \end{cases} \tag{57}$$

where $\varepsilon(y)$ is an appropriately chosen random perturbation and

$$(v,w)(0,x,y) = (v_0 = 0.1, w_0 = 1.0), \quad 0 < x < L_x,\ 0 < y < L_y. \tag{58}$$

For the numerical solution of the problem, we use an explicit finite difference method with a central difference discretization of the diffusion and advection terms. The spatial step sizes of the discrete grid are $dx = dy = 0.2$ and the time step size is $dt = 0.008$, which satisfies the stability condition for the explicit scheme. The parameter values used in the numerical simulations are given in Table 14.

θ	β	γ	a	ϕ	Le	$\tilde{u}$	Λ	H_w	u^*
0.5	20.	5.0	0.25	1.0	0.3	0.25	0.0	1.0	1.25

Table 14: Typical set of parameter values used in all the numerical simulation.

4.7. Distinct fingering states

In the numerical simulations, the instability of the front is controlled by using the Péclet number as a free parameter in system (52) while other parameters assume the values given in Table 14. Figures 18 and 19 show distinct fingering states and the transition from the regime of stable planar front to the unstable regimes (fingering with and without tip-splitting). We consider two different forms of the combustion model based on the nature of the Arrhenius kinetics, which is conditioned by the parameter, θ. The first form is related to when the nondimensional activation energy is greater than zero, i.e, $\theta > 0$ and the second form, when we assumed it to be zero, i.e. $\theta = 0$.

4.7.1. Model with Arrhenius kinetics ($\theta > 0$)

We consider the behavior of the fingering instability when $\theta = 0.5$ in the Arrhenius law (55). In this case, the Arrhenius kinetics has a temperature dependent exponential factor, which enhances the nonlinear dynamics of the problem. Figure 18 shows the temperature, oxygen and solid fuel concentrations. We see that, at a relatively large Pe value ($Pe = 1.2$), the smoldering pattern has the form of a stable planar front (Figure 18a). Decreasing the value of Pe slightly ($Pe = 0.5$) results in a cellular structure, which marks the onset of the instability (Figure 18b). It should be noted that combustion occurs only at the vicinity of the tip of the front. As Pe is further decreased, the patterns separate into distinct fingers with tip-splitting and having the characteristic feature of screening neighbouring fingers from the supply of oxygen (cf. Zik and Moses, 1999).

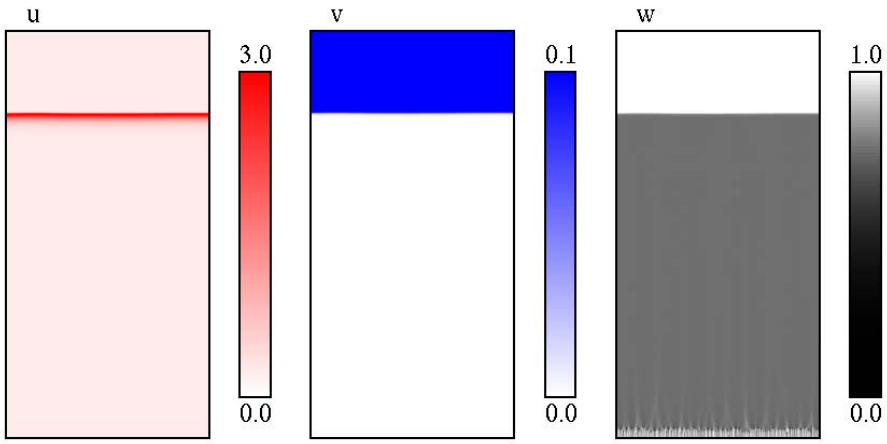

(a) Planar front at $Pe = 1.2$ ($\theta = 0.5$).

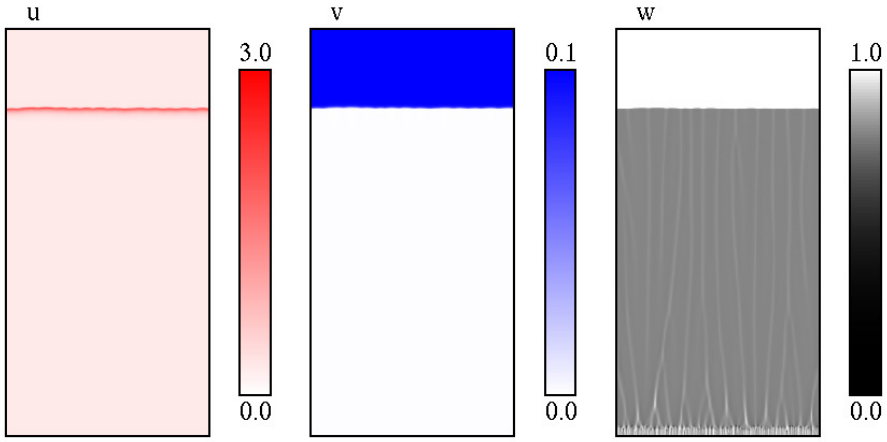

(b) Connected front with a cellular structure at $Pe = 0.5$ ($\theta = 0.5$).

Figure 18: Distribution of temperature (u), oxygen (v) and solid fuel (w) mass concentrations as a function of Pe. In the pictures, ignition is initiated from the bottom and gaseous oxidizer is passed from the top. The combustion fronts propagate from the ignition line at the bottom towards the upstream end at the top.

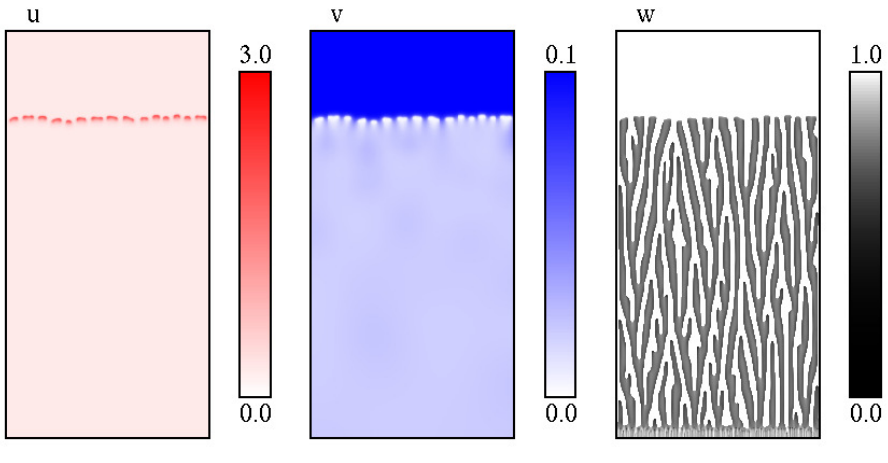

(c) Fingering patterns with tip-splitting at $Pe = 0.3$ ($\theta = 0.5$).

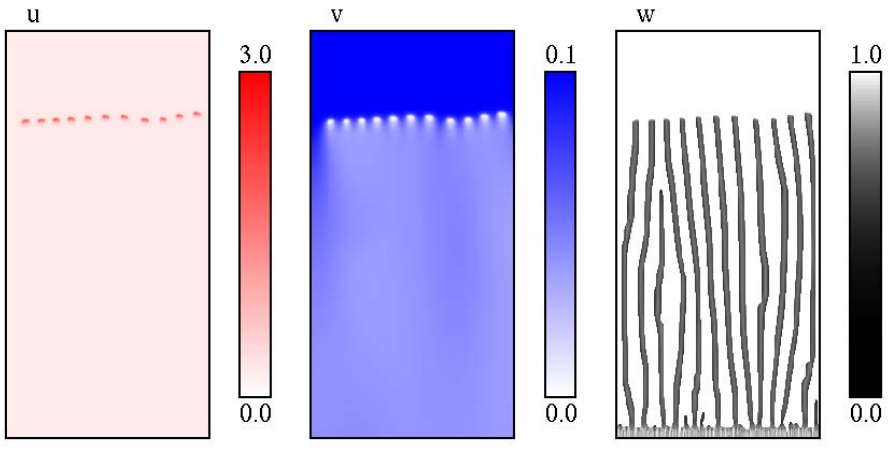

(d) Fingering pattern without tip-splitting at $Pe = 0.25$ ($\theta = 0.5$).

Figure 18: Distributions of temperature (u), oxygen (v) and solid fuel (w) concentrations in the developed fingering regime.

At $Pe = 0.25$, the emerging fingering patterns propagate as distinctly spaced fingers without tip-splitting. In this regime, the thermal front propagates in the form of isolated hot spots towards the upstream boundary. We point out that the mechanism of pattern formation demonstrated presently can also be found in the paper (Lu and Yortsos, 2005), in which a pore network simulator was employed.

4.7.2. Model with simplified Arrhenius kinetics ($\theta = 0$)

In order to ascertain the behavior of fingering patterns resulting from the system (52) with the simplified kinetics, i.e., $\theta = 0$, we examine the problem as we did earlier on.

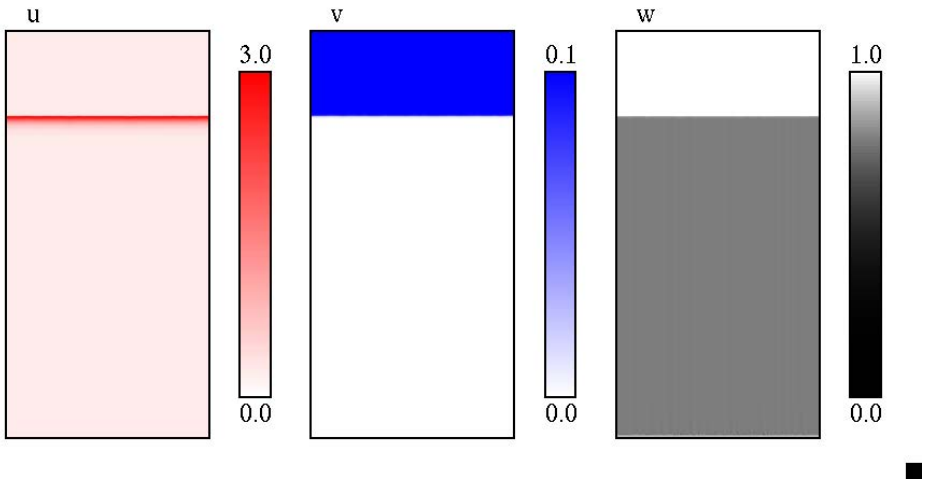

(a) Planar front at $Pe = 1.0$ ($\theta = 0.0$).

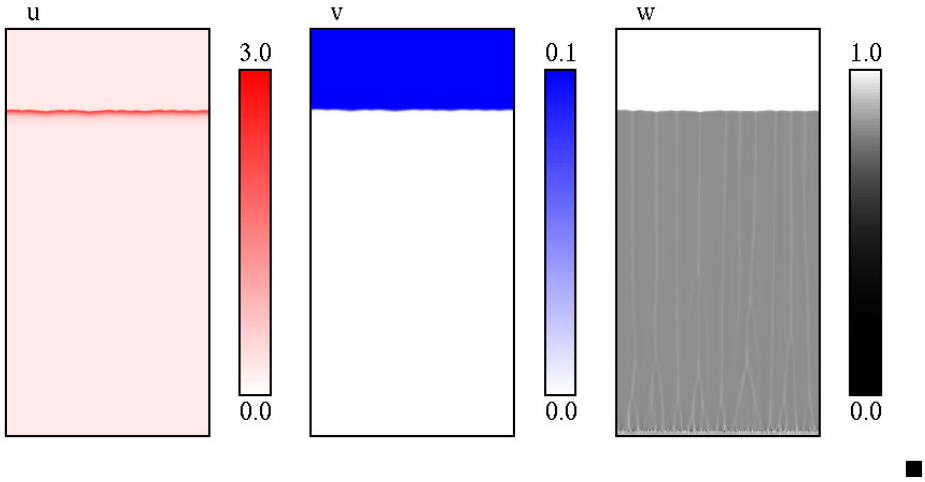

(b) Connected front with a cellular structure at $Pe = 0.45$ ($\theta = 0.0$).

Figure 19: Distribution of temperature (u), oxygen (v) and solid fuel (w) mass concentration as a function of Pe.

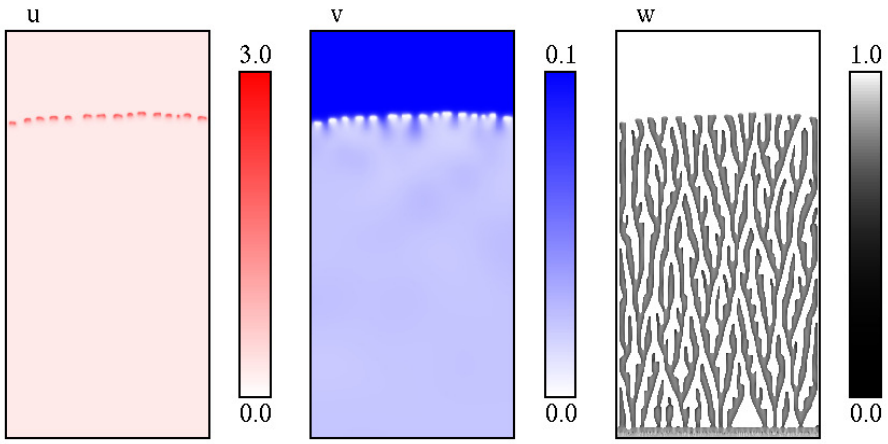

(c) Fingering pattern tip-splitting at $Pe = 0.21$ ($\theta = 0.0$).

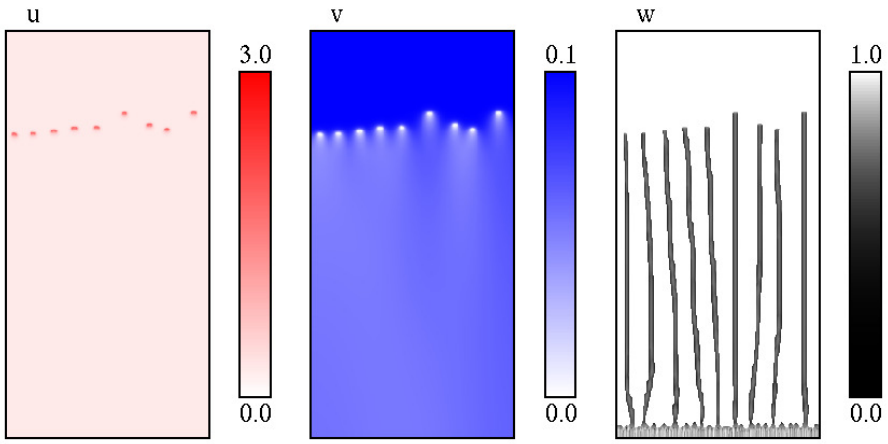

(d) Fingering pattern without tip-splitting at $Pe = 0.16$ ($\theta = 0.0$).

Figure 19: Distributions of temperature (u), oxygen (v) and solid fuel (w) concentrations in the developed fingering regime.

Figure 19 shows the distribution of temperature, oxygen and solid fuel concentrations in this case. The parameter values used in the numerical simulation are similar to those used in Figure 18. Based on the pattern-forming dynamics, the results depicted in Figure 19 show no significant difference with the results demonstrated in Figure 18. However, an obvious difference between the numerical results can be seen in the range of Pe

values, which exhibit the distinct patterns in the two models.

In connection with the phenomena of interest, we see that the model with the simplified kinetics captures similar qualitative fingering patterns. The patterns show good agreement with the dynamics of the fingering instability described in the experiments (Zik and Moses, 1999; Olson et al., 1998, 2009).

5. Conclusion

In this study, we have derived a functional form for the limit homogenized problem, which we used to establish a link to a previous phenomenological reaction-diffusion model (Ikeda and Mimura, 2008). The proposed model has the following improvements:

- Kinetic model for the solid fuel mass balance that uses a second order Arrhenius type kinetics as a consumption rate for the reactants and a production rate for the heat release mechanism. The local solid fuel conversion within the inclusions reveals distinct patterns, perceptive of the global behavior of fuel conversion in the homogenized model. It also extended the mechanism of the smoldering combustion process; specifically, the model exhibits coexistence of upstream and downstream smolder waves.

- Radiative heat transfer mechanism that accounts for the effect of heat losses from the surface of the solid and to the surroundings. It extended the range of validity of the previously proposed adiabatic model (Ijioma et al., 2013); thus, the visibility of the finger-like patterns are not impaired. Also, it brings the model to a more viable range for the emergence of steady state of fingers without tip-splitting. We showed that, with the radiative heat losses, the finger widths are narrower compared to the results of the adiabatic model reported in Ijioma et al. (2013).

We also obtained formulas for calculating the effective transport parameters in the homogenized model. The effective parameters allowed us to show the efficiency of the homogenization process in the slow smoldering regime. The results of the numerical simulations show close agreement between the homogenized solution and the microscopic solutions. We conclude that the homogenization procedure demonstrated in the present study is efficient provided that the regimes of convection and chemical reactions are constrained within the range for a slow smoldering combustion process.

Furthermore, we studied the behavior of the macroscopic system of equations numerically for the problem of fingering instability in microgravity smoldering combustion. We showed that the proposed model captures the distinct fingering states reminiscent of the experimentally observed finger-like char patterns, thus confirming the close resemblance of the pattern-forming dynamics of our model to the mechanism of diffusion instability observed in the experiment. Specifically, at a relatively low Péclet number, the proposed model predicts distinctly spaced sparse fingers without tip-splitting. The latter result is conditioned by the presence of the radiative heat losses, contrary to the predictions of the previously studied adiabatic model (see Ijioma et al., 2013).

We also analyzed the problem of fingering instability using two forms of the Arrhenius kinetics, which depend on the nondimensional activation energy, θ. It was shown that the patterns observed for $\theta = 0.5$ and $\theta = 0.0$ are qualitatively similar though the Péclet values which exhibit the patterns are slightly different. These results imply that, instead of the Arrhenius law with a temperature dependent exponential factor, one can use the model with the simplified kinetics ($\theta = 0$) since it describes the essential feature of the combustion phenomena. For example, the transition of the patterns from planar front to fingering without tip-splitting. A potential advantage of using the simplified kinetics is the ease of theoretical analysis; particularly, it is easier to treat the smoldering combustion problem from the perspective of traveling wave analysis using the simplified kinetics.

Acknowledgement

This work was supported by the Mathematical Institute for Advanced Study of Mathematical Sciences (MIMS), Center for Mathematical Modeling and Applications (CMMA), Meiji University.

References

T. Ohlemiller, D. Lucca, An experimental comparison of forward and reverse smolder propagation in permeable fuel bed, Combust. Flame 54 (1983) 131–147.

T. Ohlemiller, Modeling of smoldering combustion propagation, Progress in Energy Combust. Sci. 11 (1985) 277–310.

C. Wahle, B. Matkowsky, A. Aldushin, Effects of gas-solid nonequilibrium in filtration combustion, Combust. Sci. and Tech. 175 (2003) 1389–1499.

D. Schult, B. Matkowsky, V. Volpert, A. Fernandez-Pello, Propagation and extinction of forced opposed smolder waves, Combust. Flame 101 (1995) 471–490.

O. Zik, Z. Olami, E. Moses, Fingering instability in combustion, Phys. Rev. Lett. 81 (1998) 3868–3871.

O. Zik, E. Moses, Fingering instability in combustion: An extended view, The American Phys. Soc. 60 (1999) 518–531.

O. Zik, E. Moses, Fingering instability in combustion: The characteristic scales of the developed state, Proceeding of Combustion Institute 27 (1998) 2815–2820.

S. Olson, H. Baum, T. Kashiwagi, Finger-like smoldering over thin cellulose sheets in microgravity, Twenty-Seventh Symposium (International) on Combustion (1998) 2525–2533.

S. L. Olson, F. J. Miller, I. S. Wichman, Characterizing fingering flamelets using the logistic model, Combustion Theory and Modelling 10 (2) (2006) 323–347.

K. Kuwana, G. Kushida, Y. Uchida, Lewis number effect on smoldering combustion of a thin solid, Combust. Sci. Technol. 186 (4-5) (2014) 466–474, URL `http://dx.doi.org/10.1080/00102202.2014.883220`.

C. Lu, Y. Yortsos, Pattern formation in reverse filtration combustion, Phys. Rev. E. 72 (2005) 036201(1–16).

L. Kagan, G. Sivashinsky, Pattern formation in flame spread over thin solid fuels, Combust. Theory Model. 12 (2008) 269–281.

K. Ikeda, M. Mimura, Mathematical treatment of a model for smoldering combustion, Hiroshima Math. J. 38 (2008) 349–361.

A. Fasano, M. Mimura, M. Primicerio, Modelling a slow smoldering combustion process, Math. Methods Appl. Sci. (2009) 1–11.

E. R. Ijioma, A. Muntean, T. Ogawa, Pattern formation in reverse smouldering combustion: A homogenisation approach, Combust. Theory and Model. 17 (2) (2013) 185–223.

F.-p. Yuan, Z.-b. Lu, Structure and stability of non-adiabatic reverse smolder waves, Applied Mathematics and Mechanics (2013) 1–12.

L. Hu, C.-M. Brauner, J. Shen, G. I. Sivashinsky, Modeling and simulation of fingering pattern formation in a combustion model, Mathematical Models and Methods in Applied Sciences 25 (04) (2015) 685–720, doi: 10.1142/S0218202515500165.

E. R. Ijioma, A. Muntean, T. Ogawa, Effect of material anisotropy on the fingering instability in reverse smoldering combustion, Int. J. Heat Mass Transf. 81 (0) (2015) 924–938, ISSN 0017-9310, doi: http://dx.doi.org/10.1016/j.ijheatmasstransfer.2014.11.021.

Y. Uchida, K. Kuwana, G. Kushida, Experimental validation of Lewis number and convection effects on the smoldering combustion of a thin solid in a narrow space, Combust. and Flame (0) (2015) –, ISSN 0010-2180, doi:http://dx.doi.org/10.1016/j.combustflame.2014.12.014.

S. Whitaker, Theory and applications of transport in porous media: The method of volume averaging, vol. 13, Kluwer Academic Publishers, The Netherlands, 1998.

A. Oliveira, M. Kaviany, Nonequilibrium in the transport of heat and reactants in combustion in porous media, Progress in Energy and Combustion Science 27 (2001) 523–545.

N. Bakhvalov, G. Panasenko, Homogenisation: Averaging Processes in Periodic Media, vol. 36 of *Mathematics and its Applications (Soviet Series)*, Kluwer Academic Publishers Group, Dordrecht, 1989.

A. Bensoussan, J. L. Lions, G. Papanicolaou, Asymptotic Analysis for Periodic Structures, vol. 5 of *Studies in Mathematics and its Application*, North-Holland, 1978.

E. Sanchez-Palencia, A. Zaoui, Homogenization Techniques for Composite Media, vol. 272 of *Lecture Notes in Physics*, Springer, 1985.

U. Hornung, Homogenization and Porous Media, vol. 6 of *Interdisciplinary Applied Mathematics*, Springer-Verlag, New York, 1997.

G. Allaire, Homogenization and two-scale convergence, SIAM J. Math. Anal. 23 (6) (1992) 1482–1518.

G. Allaire, A. Damlamian, U. Hornung, Two-Scale Convergence On Periodic Surfaces And Applications, World Scientific Publishing Co. Pte. Ltd., 1995.

T. Fatima, E. Ijioma, T. Ogawa, A. Muntean, Homogenization and dimension reduction of filtration combustion in heterogeneous thin layers, Networks and Heterogeneous Media 9 (4) (2014) 709–737.

J.-L. Auriault, Macroscopic modelling of heat transfer in composites with interfacial thermal barrier, Int. J. Heat Mass Transfer 37 (18) (1997) 2885–2892.

S. Monsurro, Homogenization of a two-component composite with interfacial thermal barrier, Adv. Math. Sci. Appl. 13 (1) (2003) 43–63.

G. Allaire, K. El Ganaoui, Homogenization of a conductive and radiative heat transfer problem, Multiscale Modeling and Simulation 7 (3) (2009) 1148–1170, URL http://epubs.siam.org/doi/abs/10.1137/080714737.

G. Allaire, Z. Habibi, Homogenization of a conductive, convective, and radiative heat transfer problem in a heterogeneous domain, SIAM Journal on Mathematical Analysis 45 (3) (2013) 1136–1178.

L. Kagan, G. Sivashinsky, Incomplete combustion in nonadiabatic premixed gas flames, Physical Review E 53 (1996) 6021–6027.

L. Kagan, G. Sivashinsky, Self-fragmentation of nonadiabatic cellular flames, Combustion and Flame 108 (1-2) (1997) 220 – 226.

E. R. Ijioma, Homogenization approach to filtration combustion of reactive porous materials: Modeling, simulation and analysis, Ph.D. thesis, Meiji University, Tokyo, Japan, 2014.

F. Rogers, T. J. Ohlemiller, Cellulosic Insulation Material I. Overall Degradation Kinetics and Reaction Heats, Combust. Sci. Technol. 24 (1980) 129–137.

S. Leach, G. Rein, J. Ellzey, O. Ezekoye, J. L. Torero, Kinetic and fuel property effects on forward smoldering combustion, Combust. Flame 120 (3) (2000) 346–358.

A. P. Aldushin, A. Bayliss, B. J. Matkowsky, On the transition from smoldering to flaming, Combust. Flame 145 (2006) 579–606.

A. P. Aldushin, A. Bayliss, B. J. Matkowsky, Is there a transition to flaming in reverse smolder waves?, Combust. Flame 156 (2009) 2231–2251.

S. Turns, An Introduction to Combustion: Concepts and Applications, McGraw-Hill Series in Mechanical Engineering, McGraw-Hill, 2000.

A. Fakheri, S. Olson, The effects of radiative heat loss on microgravity flame spread, American Institute of Aeronautics and Astronautics, 220 – 226, URL http://dx.doi.org/10.2514/6.1989-504, 1989.

S. L. Olson, F. J. Miller, S. Jahangirian, I. S. Wichman, Flame spread over thin fuels in actual and simulated microgravity conditions, Combustion and Flame 156 (6) (2009) 1214–1226.